Spurious forces can dominate the vorticity budget of ocean gyres on the C-grid

Andrew F. Styles[1], **Michael J. Bell**[2], **David P. Marshall**[1], **and David Storkey**[2]

[1]Department of Physics, University of Oxford, Oxford, UK
[2]Met Office, Fitzroy Road, Exeter, UK

Key Points:

- The vorticity budget is used to identify forces spinning gyres up and down when integrated over the area enclosed by streamlines
- Spurious topographic forces and a numerical beta effect emerge from the Coriolis acceleration when using a C-grid with z-coordinates
- The identified spurious forces are significant in both an idealized gyre configuration and the Weddell Gyre in a realistic global model

Corresponding author: Andrew F. Styles, `andrew.styles@physics.ox.ac.uk`

Abstract

Gyres are prominent surface structures in the global ocean circulation that often interact with the sea floor in a complex manner. Diagnostic methods, such as the depth-integrated vorticity budget, are needed to assess exactly how such model circulations interact with the bathymetry. Terms in the vorticity budget can be integrated over the area enclosed by streamlines to identify forces that spin gyres up and down. In this article we diagnose the depth-integrated vorticity budgets of both idealized gyres and the Weddell Gyre in a realistic global model. It is shown that spurious forces play a significant role in the dynamics of all gyres presented and that they are a direct consequence of the Arakawa C-grid discretization and the z-coordinate representation of the sea floor. The spurious forces include a numerical beta effect and interactions with the sea floor which originate from the discrete Coriolis force when calculated with the following schemes: the energy conserving scheme (ENE); the enstrophy conserving scheme (ENS); and the energy and enstrophy conserving scheme (EEN). Previous studies have shown that bottom pressure torques provide the main interaction between the depth-integrated flow and the sea floor. Bottom pressure torques are significant, but spurious interactions with bottom topography are similar in size. Possible methods for reducing the identified spurious topographic forces are discussed. Spurious topographic forces can be alleviated by using either a B-grid in the horizontal plane or a terrain-following vertical coordinate.

Plain Language Summary

Gyres are large scale circulations in the world ocean that often interact with the sea floor. It is important to develop a method to assess how the representation of the sea floor in models affects gyre circulations. By calculating how model forces generate vorticity (the tendency to rotate) in the flow, we are able to determine the forces acting with and against the gyre circulation. We apply this method to results from a simplified double gyre model and the Weddell Gyre in a realistic global model. We show that spurious forces which emerge from the layout of the model grid play an important role in the presented gyre circulations. The spurious forces originate from the calculation of the Coriolis acceleration in the model. In previous studies, it has been argued that gyre circulations interact with the sea floor primarily by forming pressure gradients; here we show that contributions from pressure gradients are significant, but the spurious forces are similar in size and also emerge from interactions with the sea floor. We discuss possible approaches to reduce the identified spurious forces by considering alternative grid layouts. The spurious forces can be alleviated by using a B-grid or a terrain-following vertical coordinate.

1 Introduction

Accurately representing the sea floor has always been a challenge for the ocean modelling community. Quantifying the full influence of the sea floor on model circulations is important for both future model development and the interpretation of results from existing models. We present a diagnostic method that reveals how bottom topography influences the depth-integrated vorticity budget of general circulation models (GCMs) and we identify significant spurious forces that emerge from the discrete Coriolis force when calculated on a C-grid (Mesinger & Arakawa, 1976) using z-coordinates.

The recent article by Stewart et al. (2021) also studied the impact of bottom topography on vorticity budgets. However, the model used by Stewart et al. (2021) is a two layer isopycnal model where the bottom topography is completely contained in the lower density layer. In this article we consider models that have a higher vertical resolution and a step-like bathymetry. It is in these more commonly used models that we identify a new category of spurious forces.

The textbook theory of gyres relies on the idea of a depth-integrated vorticity budget and gyres can be classified by the leading order terms in the depth-integrated vorticity equation. For example, the Stommel (1948) gyre is dominated by wind stress curl, lateral bottom friction, and the beta effect. In another example, Niiler (1966) analytically integrated the vorticity equation over the area enclosed by gyre streamlines to study inertial gyres dominated by the wind stress curl, the advection of vorticity, and lateral bottom friction.

GCMs have a primitive momentum equation with an associated vorticity budget. By taking the curl of the depth-integrated terms from the primitive momentum equation we can calculate the corresponding terms in the model's depth-integrated vorticity equation (referred to as vorticity diagnostics hereafter). The vorticity diagnostics can then be integrated over the area enclosed by gyre streamlines to reveal the model forces responsible for spinning the gyre up and down. In this article we diagnose the vorticity budget of gyres in two case studies using the NEMO model (Madec et al., 2019). We consider a simple double gyre configuration with analytic forcing and idealized geometry which resembles a North Atlantic basin. We also consider the vorticity budget of the Weddell Gyre in a realistic configuration of the global ocean. In both of these case studies we identify spurious force profiles with different characteristics. In the light of these results, we discuss potential changes to the model discretizations that could mitigate the spurious forces.

The article is structured as follows. We first discuss the analytic depth-integrated vorticity budget in Section 2 as well as the analytic method of contour integration. In Section 3 we consider how the depth-integrated vorticity budget behaves on a C-grid with step-like bathymetry and how spurious terms emerge from the discrete Coriolis acceleration. Results from the analytically forced double gyre model are presented in Section 4 and results for the Weddell Gyre are presented in Section 5. A discussion of approaches to avoid the spurious forcing terms can be found in Section 6. Closing remarks are given in Section 7. In Appendix A we present the discrete forms of the Coriolis acceleration for various vorticity schemes. Appendix B presents results from the double gyre model using various forms of the discrete Coriolis acceleration. In Appendix C we consider a simple example of contour integration on the B-grid. Appendix D presents contour integrations of uninterpolated diagnostics from the double gyre model.

2 The analytic vorticity budget

2.1 The depth-integrated vorticity equation

Vorticity diagnostics are an underused tool for interpreting model circulations and offer a description of gyre dynamics that complements textbook theory (Vallis, 2017). A handful of recent papers have used a vorticity budget to diagnose regional GCM models (Schoonover et al., 2016; Bras et al., 2019; Le Corre et al., 2020).

To obtain a depth-integrated vorticity budget analytically we start from the vector-invariant form of the momentum equation:

$$\frac{\partial \mathbf{u_h}}{\partial t} = -\left[(\nabla \times \mathbf{u}) \times \mathbf{u} + \frac{1}{2} \nabla \left(\mathbf{u} \cdot \mathbf{u} \right) \right]_h - f \left(\hat{\mathbf{k}} \times \mathbf{u} \right)_h - \frac{1}{\rho_0} \nabla_h P + \mathcal{F}^{\mathbf{u}} + \mathcal{D}^{\mathbf{u}}, \tag{1}$$

where f is the Coriolis parameter, $\mathcal{F}^{\mathbf{u}}$ is top and bottom surface forcing, $\mathcal{D}^{\mathbf{u}}$ is the lateral diffusion of momentum, $\mathbf{u}_h$ is the 'horizontal' (parallel to the Earth's surface) velocity vector, ∇_h is the horizontal gradient operator, and $[\,\cdot\,]_h$ is the horizontal component of a vector. To derive a depth-integrated vorticity equation, we need to depth-integrate and take the curl of Equation 1. The order of the two operations and any multiplications carried out significantly alters the form and physical meaning of the obtained depth-integrated vorticity equation.

If we choose to depth-integrate the curl of the momentum equation, the pressure gradient vanishes upon taking the curl and bottom vortex stretching represents the interaction of the geostrophic currents with the sea floor. Both the beta effect and bottom vortex stretching originate from the Coriolis acceleration in Equation 1. In the model, the curl of the single momentum diagnostic associated with the Coriolis acceleration will be responsible for two distinct physical processes.

If we choose to take the curl of the depth-*averaged* momentum equation then sea floor interactions are represented by the JEBAR term (Joint Effect of Baroclinicity and Relief). Cane et al. (1998) and Drijfhout et al. (2013) have questioned the relevance of JEBAR by presenting simple examples in which there is no flow immediately above the bathymetry. In these examples there is trivially no interaction between the flow and the bathymetry, but there is a non-zero JEBAR term.

Throughout this paper we consider the vorticity equation obtained by taking the curl of the depth-integrated momentum equation:

$$\begin{aligned}\frac{\partial\overline{\zeta}}{\partial t} = \; & - \underbrace{\nabla_h \cdot (\overline{\zeta \mathbf{u}})}_{\text{Advection}} - \underbrace{\nabla_h \cdot (f\overline{\mathbf{u}})}_{\text{Planetary Vort.}} + \underbrace{\frac{1}{\rho_0}\left(\nabla P_b \times \nabla H\right)\cdot\hat{\mathbf{k}}}_{\text{Bottom pressure torque}} \\ & + \underbrace{\frac{1}{\rho_0}\left(\nabla \times \boldsymbol{\tau}_{\text{surf}}\right)\cdot\hat{\mathbf{k}}}_{\text{Surface stress curl}} - \underbrace{\frac{1}{\rho_0}\left(\nabla \times \boldsymbol{\tau}_{\text{bot}}\right)\cdot\hat{\mathbf{k}}}_{\text{Bottom friction}} + \underbrace{\mathcal{D}^{\zeta}}_{\text{Lateral diffusion}}, \end{aligned} \tag{2}$$

where ζ is the vertical component of the vorticity, $\boldsymbol{\tau}_{\text{surf}}$ is the surface stress due to wind and sea ice, $\boldsymbol{\tau}_{\text{bot}}$ is the bottom stress due to friction at the sea floor, $\mathcal{D}^{\zeta}$ is the lateral diffusion of depth-integrated relative vorticity ($= \nabla \times \overline{\mathcal{D}}^{\mathbf{u}} \cdot \hat{\mathbf{k}}$), and P_b is the pressure at the sea floor. Variables with a bar represent a depth-integrated quantity:

$$\overline{\mathbf{u}} = \int_{-H(x,y)}^{\eta(x,y,t)} \mathbf{u}_h \, dz, \tag{3}$$

where η is the free surface height, H is the depth of the sea floor, x is the zonal coordinate, and y is the meridional coordinate.

The terms on the right-hand side of Equation 2 are the following: the advection of relative vorticity; the planetary vorticity term; the bottom pressure torque; the surface stress curl; the curl of bottom friction; and the lateral diffusion of relative vorticity. The planetary vorticity term in Equation 2 contains contributions from the evolving free surface as $\nabla_h \cdot \overline{\mathbf{u}} = -\partial\eta/\partial t$. In an equilibrated state, the free surface evolution is small, and hence we assume $\nabla_h \cdot (f\overline{\mathbf{u}}) \approx \beta\overline{v}$ where β represents the linear variation of f with latitude and $\overline{v}$ is the meridional component of the depth-integrated velocity. This formulation is practical as topographic interactions emerge from pressure gradients in the form of the bottom pressure torque and beta effects emerge from the curl of the Coriolis acceleration; the Coriolis acceleration is responsible for one physically meaningful term in the analytic vorticity budget. Equation 2 is also used in Stewart et al. (2021).

As a consequence of Stokes' theorem, the area integral of a term from Equation 2 is directly related to the line integral of the depth-integrated forces along the area edge. This is particularly useful when considering area integrals of terms from the vorticity equation and is discussed further in the next sub-section.

2.2 Contour integration method

All terms in the depth-integrated vorticity equation can be expressed as the curl of a depth-integrated acceleration in the momentum equation:

$$\overline{\Omega} = \left(\nabla \times \overline{\mathbf{M}}\right)\cdot\hat{\mathbf{k}}, \tag{4}$$

where $\overline{\Omega}$ is a term in the depth-integrated vorticity equation and $\overline{\mathbf{M}}$ is a term in the depth-integrated momentum equation. If we integrate $\overline{\Omega}$ over the area enclosed by a depth-integrated streamline, we can interpret the integral using Stokes' theorem:

$$I(\psi) = \pm \iint_{A_\psi} \overline{\Omega}\, dA = \pm \oint_{\Gamma_\psi} \overline{\mathbf{M}} \cdot \mathbf{dl}, \tag{5}$$

where A_ψ is the area enclosed by a depth-integrated streamline and Γ_ψ is the anticlockwise path along the same streamline. The criteria for selecting the sign in Equation 5 is defined later in this paragraph. The integral $I(\psi)$ can be interpreted as the work done per unit mass by the force associated with $\mathbf{M}$ on a fluid column in one circulation of Γ_ψ. For a gyre circulating in a clockwise direction, the direction of circulation would be opposite to the conventional anticlockwise direction of Γ_ψ. So that the reader does not have to constantly consider the direction of the flow relative to Γ_ψ we select the sign in Equation 5 so a positive value of $I(\psi)$ corresponds to a force that is spinning the gyre up.

Analytically, we would expect the planetary vorticity term to vanish upon integration as a consequence of the divergence theorem:

$$\iint_{A_\psi} \nabla \cdot (f\overline{\mathbf{u}})\; dA = \oint_{\Gamma_\psi} f\overline{\mathbf{u}} \cdot \hat{\mathbf{n}}\, dl = 0, \tag{6}$$

where $\hat{\mathbf{n}}$ is the horizontal vector which is normal to the streamline and the depth-integrated velocity. The Coriolis force can still play a role in shaping the streamlines of the circulation but ultimately has no influence on the integrated budget. Although the advection term, $\nabla_h \cdot \left(\overline{\mathbf{u}\zeta}\right)$, has a similar form, we do not expect the same zero integral for the advection term as $\overline{\mathbf{u}\zeta}$ is not parallel to $\overline{\mathbf{u}}$ in general.

This method has been used in models before. Schoonover et al. (2016) integrated vorticity diagnostics over a limited number of streamlines in the North Atlantic and concluded that wind stress curl is largely balanced by bottom pressure torques. Stewart et al. (2021) also used this method in an isopycnal model and concluded that wind stress curl is not balanced by bottom pressure torques in general. Stewart et al. (2021) discuss how the integrating area affects the resultant vorticity balances and in their model the wind stress curl is only balanced by bottom pressure torques when integrated over latitude bands. It should be noted that Schoonover et al. (2016) and Stewart et al. (2021) use terrain-following coordinates in their models but in this article we study the vorticity budget of a z-coordinate model. In Section 6.3 we discuss how the vorticity budget can be affected by the choice of vertical coordinate and how terrain-following coordinates can mitigate spurious Coriolis forces related to the topography.

3 The vorticity budget on a C-grid

3.1 The discrete depth-integrated vorticity equation

In NEMO, and many other contemporary ocean GCMs, the discretized model variables are distributed on the C-grid (Mesinger & Arakawa, 1976). The geometry of the C-grid is shown in Figure 1: T points hold scalar information including the divergence of the flow; the U and V points hold the horizontal components of vector quantities including the horizontal velocity, surface stresses, and accelerations in the momentum equation ($\mathbf{M}$). Values closely related to vorticity are found on F points, this includes the relative vorticity, the Coriolis parameter, the streamfunction, and terms in the depth-integrated vorticity equation ($\overline{\Omega}$). Vertical velocities are located on W points that are directly above and below T points as shown in Figure 1.

Every point in the C-grid has an associated cell with a vertical thickness and horizontal width. Throughout this article e^{3t} is the T cell vertical thickness and e^{1t}, e^{2t} are the T cell widths in the i and j direction respectively. The same convention is used for

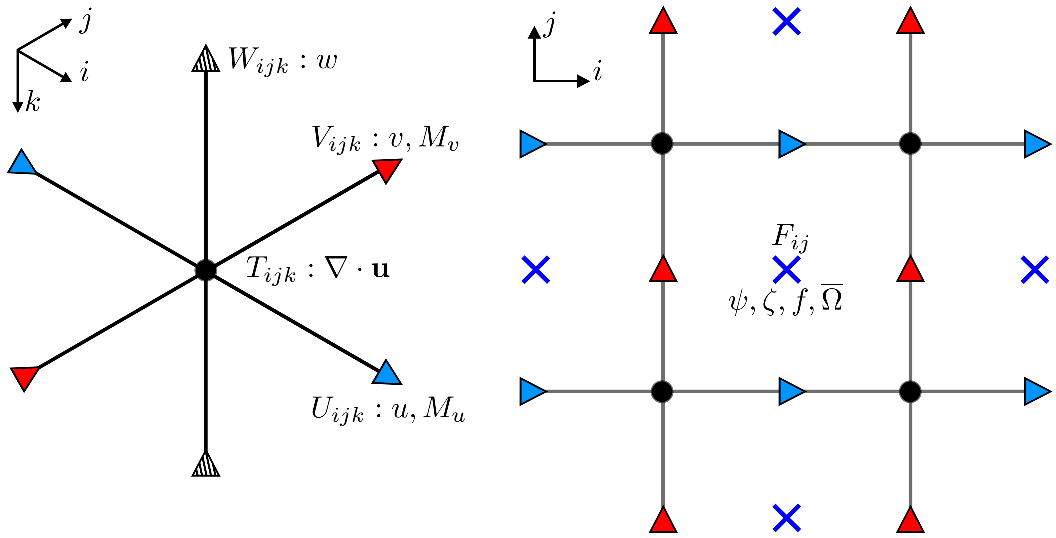

Figure 1. The distribution of variables on the C-grid in both a three dimensional (left) and horizontal (right) view. The T, U, V, F, and W points are shown alongside important values that are centred on these points. The variable w is the vertical velocity and M_u, M_v are the x and y components of a term in the momentum equation. Note that k increases downwards whilst z increases upward to match the NEMO model convention.

U, V, and F cells also. It should be noted that the values of the F cell thicknesses in this article depend on the scheme used to calculate the Coriolis acceleration (see Section 3.2).

The GCM configurations discussed in this paper use a primitive momentum equation that is a discrete equivalent to the vector invariant momentum equation (Madec et al., 2019). Momentum diagnostics can be combined to represent terms in the analytic momentum equation (Equation 1). The curl of the depth-integrated momentum diagnostics is taken to form a closed discrete vorticity budget that is valid in an unsteady state as the time derivative diagnostic is included. The resultant vorticity diagnostics should closely resemble the terms in the depth-integrated vorticity equation (Equation 2); however, the planetary vorticity diagnostic deviates from the planetary vorticity *term* in several significant ways.

3.2 The discrete Coriolis acceleration

The Coriolis acceleration is a product of the Coriolis parameter, f, and the velocity $\mathbf{u}$. Here f and $\mathbf{u}$ are located at different points on the C-grid so there are many possible schemes for calculating their cross product and the choice of scheme affects the quantities that are conserved in the model flow. Mainstream schemes use multi-point and thickness-weighted averaging of f and $\mathbf{u}$ (Madec et al., 2019). A general form of the discrete Coriolis acceleration under these schemes is:

$$\mathrm{COR}^x_{i,j,k} = \sum_{n=1}^{N} \frac{1}{N} \frac{1}{e^{1u}_{i,j}} \left(\frac{f(\mathbf{a_n})}{e^{3f}_k(\mathbf{b}_n)} \right) \tilde{V}_k(\mathbf{c_n}),$$
$$\mathrm{COR}^y_{i,j,k} = \sum_{n=1}^{N} \frac{-1}{N} \frac{1}{e^{2v}_{i,j}} \left(\frac{f(\mathbf{a_n})}{e^{3f}_k(\mathbf{b}_n)} \right) \tilde{U}_k(\mathbf{c_n}), \tag{7}$$

where $\mathbf{a}_n$, $\mathbf{b}_n$, and $\mathbf{c}_n$ are the horizontal locations of three neighbouring points (not necessarily different) for the n^{th} term of the sum. The terms $\tilde{V} = ve^{1v}e^{3v}$ and $\tilde{U} = ue^{2u}e^{3u}$ are volume fluxes; N is the number of terms in the average; and COR^x (COR^y) is the x (y) component of the Coriolis acceleration.

In this article we consider three popular schemes for calculating the Coriolis acceleration. The energy conserving scheme (ENE) (Sadourny, 1975) conserves total horizontal kinetic energy and uses a four point average (N=4). The enstrophy conserving scheme (ENS) (Sadourny, 1975) conserves potential enstrophy and has eight terms (N=8). Finally the energy and enstrophy conserving scheme (EEN) (Arakawa & Lamb, 1981) conserves both horizontal kinetic energy and potential enstrophy and uses a twelve point average (N=12). The explicit forms of the ENE, ENS, and EEN schemes for the Coriolis acceleration are given in Appendix A. The results in Section 4 and 5 use the EEN scheme; however, in Section 6.1 we argue that all three schemes produce similar spurious forces. This argument is more concise when we use a form of the Coriolis acceleration that is general to the ENE, ENS, and EEN schemes.

We identify deviations from the analytic value of the Coriolis acceleration by considering linear variations of f and e^{3f} near the U and V points. Expansions around the U and V points are used for COR^x and COR^y respectively:

$$f(\mathbf{r}) = f^u_{i,j} + \boldsymbol{\beta} \cdot \left(\mathbf{r} - \mathbf{r}^u_{i,j}\right) = f^v_{i,j} + \boldsymbol{\beta} \cdot \left(\mathbf{r} - \mathbf{r}^v_{i,j}\right), \tag{8}$$

$$e^{3f}_k(\mathbf{r}) = \frac{1}{\alpha(\mathbf{r})}\left[e^{3u}_{i,j,k} + \boldsymbol{\mu} \cdot \left(\mathbf{r} - \mathbf{r}^u_{i,j}\right)\right] = \frac{1}{\alpha(\mathbf{r})}\left[e^{3v}_{i,j,k} + \boldsymbol{\mu} \cdot \left(\mathbf{r} - \mathbf{r}^v_{i,j}\right)\right], \tag{9}$$

where f^u (f^v) is the value of the Coriolis parameter centred on the U (V) point; $\boldsymbol{\beta}$ is a vector describing the local horizontal gradient of f; $\boldsymbol{\mu}$ is a vector describing the local horizontal gradient of F cell thicknesses; $\mathbf{r}$ is a general horizontal point; $\mathbf{r}^u_{i,j}$ ($\mathbf{r}^v_{i,j}$) is the horizontal location of the U (V) point with the coordinate (i, j). We assume that the local domain for calculating the Coriolis force is small enough for a linear approximation of the Coriolis parameter and the bathymetry to be valid. We do not assume the same for $\alpha(\mathbf{r}) \sim 1$ which represents sudden changes in e^{3f} that only occur in the EEN scheme. In the EEN scheme:

$$e^{3f}_{i,j,k} = \frac{1}{4}\left(e^{3t}_{i,j,k} + e^{3t}_{i+1,j,k} + e^{3t}_{i,j+1,k} + e^{3t}_{i+1,j+1,k}\right), \tag{10}$$

where masked T cell thicknesses are set to zero. Equation 10 can produce sudden changes in F cell thicknesses near bathymetry. Sudden changes in e^{3f} are unique to the EEN scheme so $\alpha = 1$ in the ENS and ENE cases. The ENS and ENE schemes have an alternative definition of e^{3f} found in Appendix A.

By combining Equations 7, 8, and 9 we can derive a general decomposition of the Coriolis acceleration:

$$\begin{aligned}\mathrm{COR}^x_{i,j,k} = {} & \sum_{n=1}^{N} \frac{f^u_{i,j}}{N} \frac{\tilde{V}_{\mathbf{b}_n,k}}{\left(e^{1u}e^{3u}\right)_{i,j,k}} \Bigg[1 + \underbrace{\frac{\boldsymbol{\beta}}{f^u_{i,j}} \cdot \left(\mathbf{a}_n - \mathbf{r}^u_{i,j}\right)}_{\text{Num. beta}} \\ & + \underbrace{\left[\alpha(\mathbf{b}_n) - 1\right] - \alpha(\mathbf{b}_n)\boldsymbol{\mu} \cdot \left(\mathbf{b}_n - \mathbf{r}^u_{i,j,k}\right)}_{\text{Topographic}} + \underbrace{\left[\alpha(\mathbf{b}_n) - 1\right] \frac{\boldsymbol{\beta}}{f^v_{i,j}} \cdot \left(\mathbf{a}_n - \mathbf{r}^u_{i,j}\right)}_{\text{Coupled beta-topo}}\Bigg],\end{aligned} \tag{11}$$

$$\begin{aligned}\mathrm{COR}^y_{i,j,k} = {} & \sum_{n=1}^{N} \frac{-f^v_{i,j}}{N} \frac{\tilde{U}_{\mathbf{b}_n,k}}{\left(e^{2v}e^{3v}\right)_{i,j,k}} \Bigg[1 + \underbrace{\frac{\boldsymbol{\beta}}{f^v_{i,j}} \cdot \left(\mathbf{a}_n - \mathbf{r}^v_{i,j}\right)}_{\text{Num. beta}} \\ & + \underbrace{\left[\alpha(\mathbf{b}_n) - 1\right] - \alpha(\mathbf{b}_n)\boldsymbol{\mu} \cdot \left(\mathbf{b}_n - \mathbf{r}^v_{i,j,k}\right)}_{\text{Topographic}} + \underbrace{\left[\alpha(\mathbf{b}_n) - 1\right] \frac{\boldsymbol{\beta}}{f^v_{i,j}} \cdot \left(\mathbf{a}_n - \mathbf{r}^v_{i,j}\right)}_{\text{Coupled beta-topo}}\Bigg].\end{aligned} \tag{12}$$

The Coriolis acceleration has a zeroth order contribution centred on the U or V point. The unmasked (see Section 3.3) zeroth order term matches the analytic form of the Coriolis acceleration as it is the analytic value of f centred on the U point (V point) multiplied by the point-averaged value of v ($-u$) centred on the U point (V point).

The remaining terms are first order departures from the analytic value of the Coriolis acceleration. The first order contributions are: a numerical beta effect caused by deviations of the point-averaged f from its analytic value at the U or V point; a topographic effect caused by variations in F cell thicknesses; and a coupled beta-topographic effect caused by the combined effect of sudden changes in cell thicknesses and the previously mentioned numerical beta effect. Note that if $\alpha = 1$ (true for ENS and ENE) then the beta-topographic effect vanishes.

The depth-integrated Coriolis acceleration is:

$$\overline{\mathrm{COR}}^x_{i,j} = \sum_{k=1}^{k^x_{max}(i,j)} e^{3u}_{i,j,k} \mathrm{COR}^x_{i,j,k}, \tag{13}$$

$$\overline{\mathrm{COR}}^y_{i,j} = \sum_{k=1}^{k^y_{max}(i,j)} e^{3v}_{i,j,k} \mathrm{COR}^y_{i,j,k}, \tag{14}$$

where $k^x_{\max}$ and $k^y_{\max}$ are the highest unmasked indices in the column and they may vary with horizontal index when z-coordinates are used. The depth-integrated Coriolis acceleration is therefore also sensitive to steps in the bathymetry. This is discussed in the next sub-section.

3.3 The influence of model level steps on the Coriolis acceleration

In this section, we present a toy configuration that highlights how model levels can influence the discrete Coriolis acceleration. The configuration is shown in Figure 2. The configuration has two model levels, three U-grid points in the i direction, two in the j direction, and a rigid lid. The points in the upper level are surrounded by unmasked points, we assume the grid is regular, and cell widths are the same in the i and j direction. We also assume an f-plane so f does not vary.

The configuration has a step bathymetry and a current running alongside it. The current has no y component so $v = 0$ everywhere and therefore $\mathrm{COR}^x = 0$ at all points. The lower limb of the current decelerates by an amount U_1 and as a consequence of incompressibility a vertical velocity is induced which accelerates the upper current by U_1.

Under these assumptions, the discrete Coriolis acceleration does not vary between the ENE, ENS, and EEN schemes and is:

$$\mathrm{COR}^y_{i,j,k} = \frac{f}{4}\left[u_{i,j,k} + u_{i-1,j,k} + u_{i,j+1,k} + u_{i-1,j+1,k}\right], \tag{15}$$

which is effectively f multiplied by the four point average of u.

In the upper layer, the Coriolis accelerations, located on the V points marked by red triangles in Figure 2, are:

$$\mathrm{COR}^y_{1,1,k=1} = fU_0, \tag{16}$$

$$\mathrm{COR}^y_{2,1,k=1} = \frac{f}{4}\left(4U_0 + U_1\right). \tag{17}$$

In the lower layer, the Coriolis accelerations are set to zero as they lie on masked V points. The V points are masked to prevent accelerations into the topography that would violate the no penetration boundary condition. The depth-integrated Coriolis accelerations

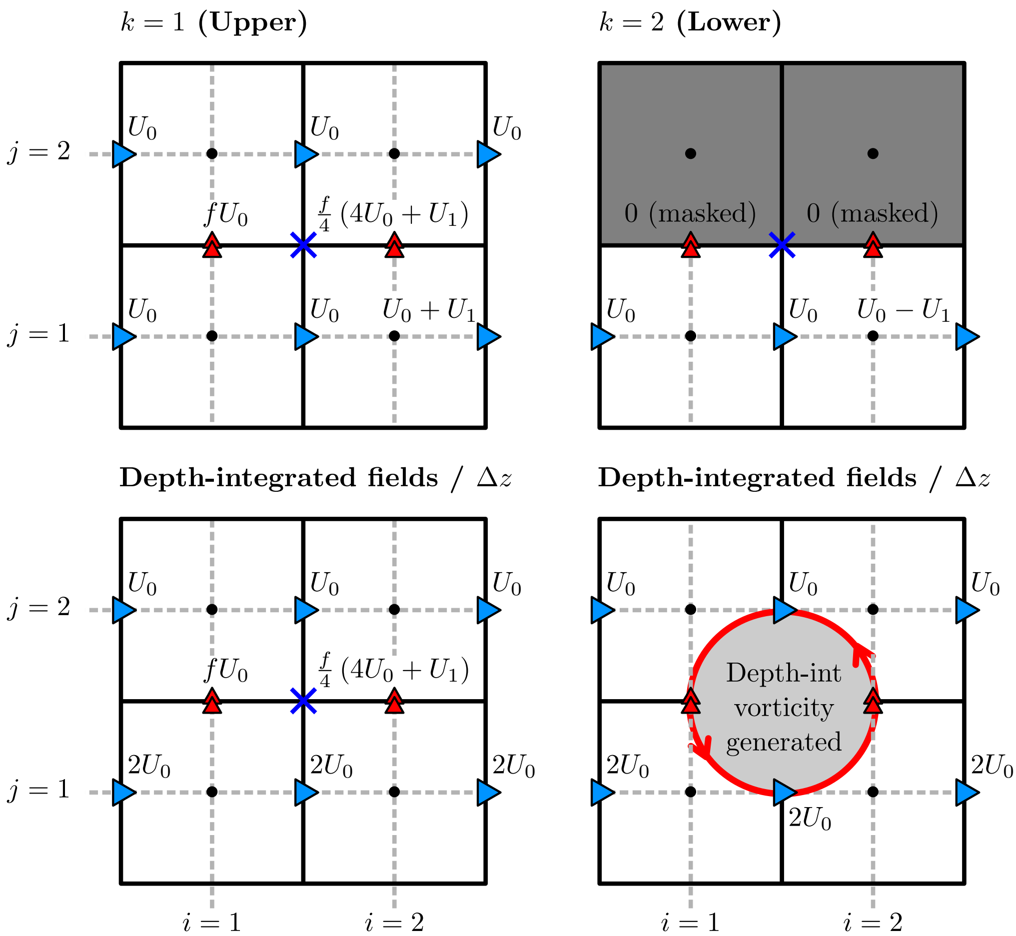

Figure 2. A toy model demonstrating how model levels influence the discrete Coriolis acceleration. A horizontal plan is shown for the upper and lower level as well as a view of the depth-integrated fields divided through by the cell thickness Δz. Single arrows represent prescribed velocities; double arrows represent calculated Coriolis accelerations; and shaded cells represent bottom topography. Accelerations on the lower level are masked to prevent the velocity field from evolving into a flow that would violate the no penetration boundary condition. The central F point is marked by a cross and is where the depth-integrated vorticity is generated.

are:

$$\overline{\mathrm{COR}}^{y}_{1,1} = \mathrm{COR}^{y}_{1,1,k=1}\,\Delta z, \tag{18}$$

$$\overline{\mathrm{COR}}^{y}_{2,1} = \mathrm{COR}^{y}_{2,1,k=1}\,\Delta z, \tag{19}$$

where Δz is the constant cell thickness. It should be noted that U_1 vanishes when calculating the depth-integrated velocities but remains in the depth-integrated acceleration. The depth-integrated Coriolis acceleration depends on more than the depth-integrated velocities.

When we take the curl of the depth-integrated accelerations, we can see how a depth-integrated vorticity is generated:

$$\frac{1}{\Delta x}\left[\overline{\mathrm{COR}}^{y}_{2,1} - \overline{\mathrm{COR}}^{y}_{1,1}\right] = \frac{1}{4}\frac{\Delta z}{\Delta x} f U_1, \tag{20}$$

where Δx is the constant cell width. Note that this value is located on the central F point shown in Figure 2.

The masking of the Coriolis accelerations on the lower level introduces a spurious force which exactly opposes the Coriolis force near topography. Pressure gradients are ambiguous on V points near bathymetry, so an explicit force balance cannot be resolved. The spurious forcing that emerges from the masking can be considered as an inferred response of the pressure field to the Coriolis acceleration near the topography. There are two possible interpretations of the result in Equation 20. We can think of the result as either the curl of an inferred pressure gradient near the bathymetry or as a form of vortex stretching that takes place on F points near model level steps (Bell, 1999).

3.4 Decomposing the planetary vorticity term

The planetary vorticity diagnostic is sensitive to variations in the Coriolis parameter, cell thicknesses, model level steps, and the divergence of the depth-integrated flow. The magnitude of these contributions may vary significantly between configurations so a general method for decomposing the planetary vorticity diagnostic is valuable. In order to effectively decompose the Coriolis acceleration, it is useful to perform variations of NEMO's calculation of the Coriolis acceleration under three different assumptions. In one calculation we impose cell thicknesses that do not vary horizontally; in another calculation we impose a constant Coriolis parameter; and in the final calculation we impose cell thicknesses that do not vary horizontally and a constant Coriolis parameter.

We then take the curl of the three depth-integrated accelerations to calculate three variations of the planetary vorticity diagnostic. The planetary vorticity diagnostics under all three assumptions include zeroth order contributions from model level changes and divergences in the depth-integrated flow ($f\nabla_h\cdot\overline{\mathbf{u}}$). The divergence of the flow over four T cells is also calculated separately. These three variations of the planetary diagnostic, the divergence contribution, and the complete planetary vorticity diagnostic are linearly combined to calculate five components of the planetary vorticity diagnostic:

- the divergence of the depth-integrated flow;
- the beta effect;
- the influence of model level steps;
- the influence of partial cells;
- the coupled beta-topographic effect.

From the analytic form $\nabla_h\cdot(f\overline{\mathbf{u}})$, we would expect contributions from the divergence and the beta effect but the remaining contributions are purely numeric. The beta effect component contains a real part that arises from spatial variations of the analytic value of f and a numerical part that arises from the difference between the point-averaged

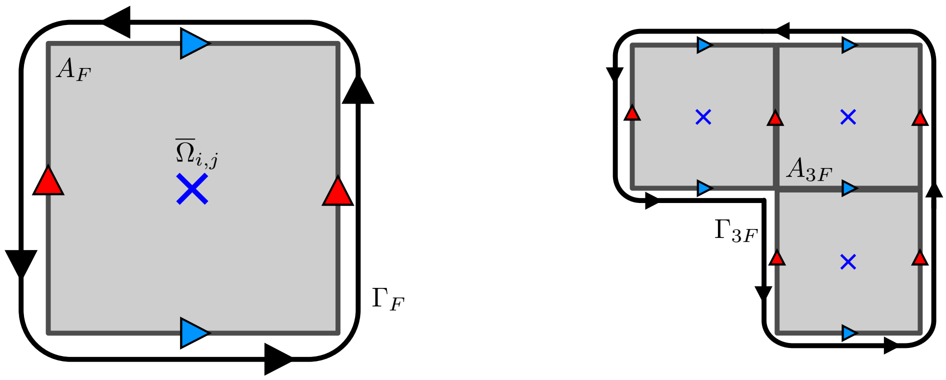

$\overline{\Omega}_{i,j} = \frac{1}{A_F} \iint_{A_F} \nabla \times \overline{\mathbf{M}} \cdot \hat{\mathbf{k}}\, dA$
$\overline{\Omega}_{i,j} = \frac{1}{A_F} \oint_{\Gamma_F} \overline{\mathbf{M}} \cdot \mathbf{dl}$

$I_{3f} = \iint_{A_{3F}} \nabla \times \overline{\mathbf{M}} \cdot \hat{\mathbf{k}}\, dA$
$I_{3F} = \oint_{\Gamma_{3F}} \overline{\mathbf{M}} \cdot \mathbf{dl}$

Figure 3. The application of Stokes' theorem on a C-grid. The vorticity diagnostic $\overline{\Omega}$ is equivalent to the normalized line integral of $\overline{\mathbf{M}}$ around a single F cell of area A_F. The area integral of $\overline{\Omega}$ over a collection of F cells (e.g. A_{3F}) is equivalent to the line integral of $\overline{\mathbf{M}}$ along the perimeter (e.g. Γ_{3F}).

value of f and its analytic value. The coupled beta-topographic component contains higher order terms as it is calculated by finding the difference between the complete planetary vorticity diagnostic and the sum of the four other components; therefore, the five components add up to the complete planetary vorticity diagnostic by construction.

3.5 Contour integration on a C-grid

Calculating the curl on a C-grid is consistent with Stokes' law applied to an F cell, and integrating $\nabla \times \overline{\mathbf{M}} \cdot \mathbf{k}$ over several adjacent F cells is equivalent to a line integral of $\overline{\mathbf{M}}$ around them (see Figure 3). As the streamfunction ψ is defined on F points we can argue that the area enclosed by a streamline is a collection of F cells and that the area integral of vorticity diagnostics is the work done by model forces in one circulation around them.

Analytically, the planetary vorticity term vanishes upon contour integration. In this section we determine whether this mathematical identity carries over to the C-grid by considering the simple configuration shown in Figure 4. We consider a depth-integrated flow on a C-grid made up of four F cells in the i direction and three in the j direction. The grid is regular and cell widths in the i and j direction are the same. There are no topographic effects as the system has no partial cells or masked points. The outer edge of the domain is a rectangular streamline, ψ_{ext}, which no flow can pass through. The interior flow follows the inside edge of ψ_{ext} and has a base velocity of U_0. A recirculation on the left intensifies the interior flow by an amount U_1. The velocity field is incompress-

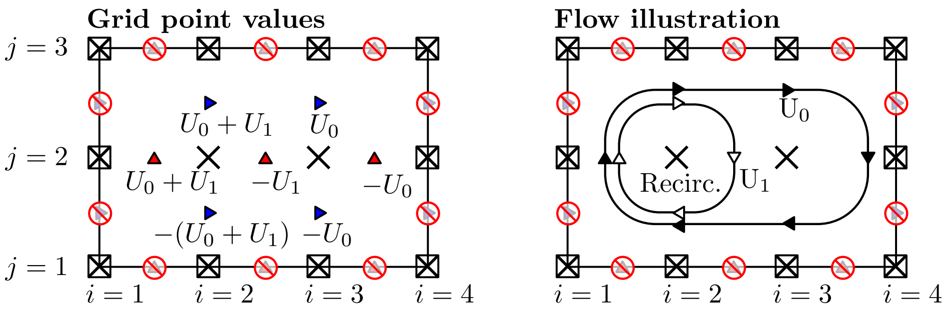

Figure 4. A simple flow where the planetary vorticity diagnostic does not integrate to zero when integrated within streamlines. The box is a rectangular streamline of value ψ_{ext} and no flow is permitted to pass through it. The depth-integrated flow is prescribed and incompressible. The grid point values of the depth-integrated velocity are given on the left and an illustration of the background flow and recirculation are given on the right.

ible and summarized below:

$$
\begin{aligned}
\overline{u}_{1,j} = \overline{u}_{4,j} &= 0, \\
\overline{u}_{2,3} = -\overline{u}_{2,2} &= U_0 + U_1, \\
\overline{u}_{3,3} = -\overline{u}_{3,2} &= U_0, \\
\overline{v}_{i,1} = \overline{v}_{i,3} &= 0, \\
\overline{v}_{2,2} &= U_0 + U_1, \\
\overline{v}_{3,2} &= -U_1, \\
\overline{v}_{4,2} &= -U_0,
\end{aligned}
$$

where we assume $U_0, U_1 > 0$. In this case the circulation is clockwise so the interior values of the streamfunction will be larger than ψ_{ext}. The minimum interior value of the streamfunction is ψ_{int}. The area enclosed by a streamline ψ where $\psi_{ext} < \psi < \psi_{int}$ is made up of the two interior F cells at $(2, 2)$ and $(3, 2)$. Using the form of the depth-integrated planetary vorticity diagnostic, $\overline{\text{PVO}}$, for the EEN scheme (derived and presented in Equation A12 in Appendix A) we can determine the value of the area integral:

$$
\begin{aligned}
I(\psi) &= (\Delta x)^2 \left[\overline{\text{PVO}}_{1,1} + \overline{\text{PVO}}_{2,1} \right], \\
&= \frac{U_1 \Delta x}{12} \left[(f_{1,2} - f_{1,0}) + (f_{2,2} - f_{2,0}) \right],
\end{aligned}
\tag{21}
$$

where PVO is the planetary vorticity diagnostic and Δx is the constant cell width. Equation 21 describes a numerical beta effect that only acts on the recirculation part of the flow. The presented example is highly idealized but it simply demonstrates that the planetary vorticity diagnostic does not generally vanish when integrated within streamlines.

4 A double gyre model

4.1 Details of the configuration

The first experiment in this article is an idealized double gyre configuration based on the GYRE PISCES reference configuration in NEMO. The GYRE PISCES reference configuration has been used for a wide range of experiments (Lévy et al., 2010, 2015; Ruggiero et al., 2015; Perezhogin, 2019). The domain is a closed rectangular basin which is 3180 km long, 2120 km wide, and is rotated at an angle of 45° relative to the zonal direction. The basin exists on a beta plane where f varies linearly around its value at $\sim 30°$N.

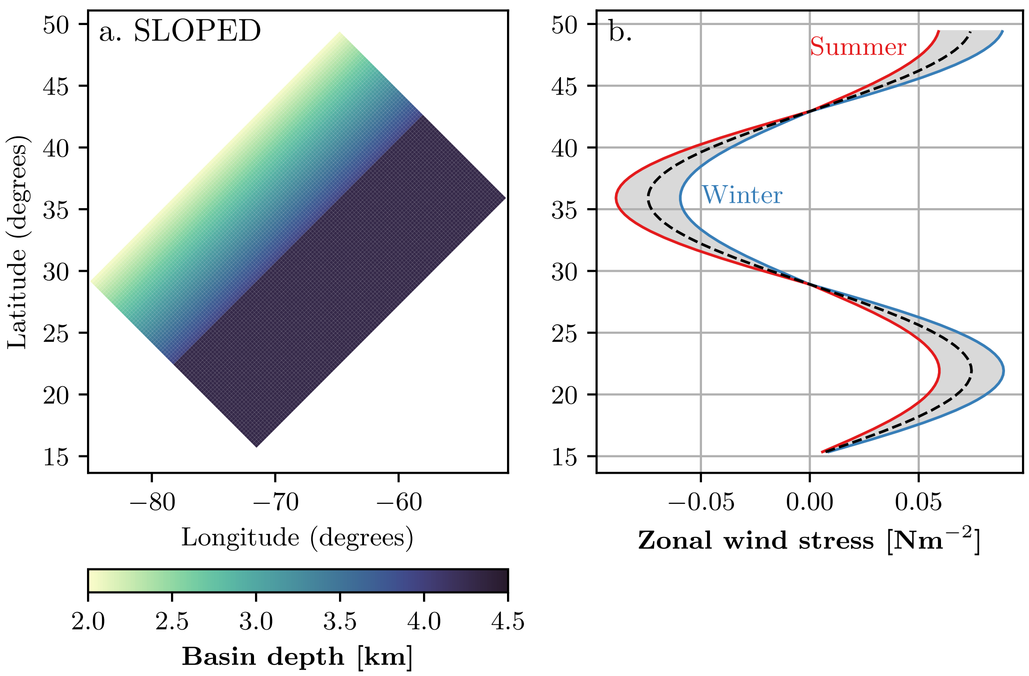

Figure 5. (a) Bathymetry of the SLOPED configuration. (b) The wind stress profile for both the FLAT and SLOPED configuration. The wind stress profile varies seasonally in a sinusoidal manner between summer and winter extremes that are highlighted.

The model has a regular 122×82 grid that is aligned with the rotated basin. The horizontal resolution is equivalent to a 1/4° grid at the equator and the configuration has 31 model levels. Two forms of bathymetry are used in this section. The FLAT configuration has a fixed depth of 4.5km and no partial cells are used. The SLOPED configuration has a linear slope that extends from the North West side of the basin and spans half the basin (see Figure 5a). The maximum depth of the SLOPED configuration is 4.5km and the minimum depth is 2km and partial cells are used to represent the slope.

The circulation is forced by sinusoidal analytic profiles of surface wind stress and buoyancy forcing. The wind stress is zonal and only varies with latitude so that the curl changes sign at 22°N and 36°N (see Figure 5b). The wind stress profile is designed to spin up a subpolar gyre in the north, a subtropical gyre in the south, and a small recirculation also emeges in the bottom corner. The wind stress and buoyancy forcing varies seasonally in a sinusoidal manner.

The model uses a free slip condition on all boundaries except at the bottom where a linear friction drag is applied. A simplified linear equation of state is used with a thermal expansion coefficient of $a_0 = 2\times10^{-4}$kg m^{-3} K^{-1}, and a haline coefficient of $b_0 = 7.7\times10^{-4}$kg m^{-3} psu^{-1}. Horizontal and biharmonic diffusion of momentum is implemented with a diffusivity of 5×10^{10} m^{4}s^{-1}. Biharmonic diffusion of tracers along isopycnals is implemented with a diffusivity of 10^9 m^{4}s^{-1}.

The model is spun up for 60 years and the experiment was run for an additional 10 years with monthly-mean outputs. A steady state is not required for this diagnostic method to work as the time derivative term is present in the vorticity budget. A time step of 10 minutes is used for the model integration.

The EEN vorticity scheme is used for consistency with all analysis discussed in Section 3 and the results from the Weddell Gyre in Section 5. The EEN method calculates F cell thicknesses using the method described by Equation 10 and we therefore expect sudden changes in the F cell thickness near the domain edge for both the FLAT and SLOPED configurations.

4.2 Methods

Momentum diagnostics are calculated for every time step and the discrete vorticity diagnostics are calculated by depth-integrating the momentum diagnostics and taking the curl. The resultant diagnostics are time-averaged over the ten year experimental period. The extensive time-averaging will influence the advection vorticity diagnostic as there is an added contribution from the eddy vorticity flux.

For contour integration, the vorticity diagnostics are then linearly interpolated onto a regular 1/12° grid. This is to minimise edge effects when carrying out the contour integrals but integrations without interpolation are similar in form (see Appendix D for an example). The depth-integrated streamfunction is calculated and also interpolated onto a regular 1/12° grid for the contour integration.

For 1001 values of ψ, closed streamline contours are identified using a marching squares algorithm from the scikit-image package (Van Der Walt et al., 2014). Streamlines that are near the recirculation gyre (south of 20°N) are ignored in this experiment and for some values of ψ no closed streamlines could be found. For each closed streamline found, the vorticity diagnostics are integrated over the area enclosed; this is equivalent to calculating $I(\psi)$ in Equation 5 over many values of ψ.

Multiple closed contours can be found for the same value of ψ so an additional contour constraint is needed to ensure $I(\psi)$ is single-valued. In this experiment we always choose the contour that spans the largest area when necessary which minimises the influence of small pocket circulations that are not a part of the gyre. Closed streamlines that run along the edge of the domain can be hard to identify so a discontinuity in $I(\psi)$ near $\psi = 0$ is expected as the largest detected contours will suddenly become pocket circulations as ψ approaches zero.

4.3 Results

The depth-integrated streamfunction from the FLAT and SLOPED configurations is shown in Figure 6. In both configurations a subtropical and subpolar gyre can clearly be identified and a small recirculation gyre can be found in the Southernmost corner. The subtropical gyre circulation is clockwise and the subpolar gyre circulation is anti-clockwise.

In the FLAT configuration the subtropical gyre has a transport of 68 Sv and the subpolar gyre has a transport of 18 Sv. In the SLOPED configuration the subtropical gyre has a transport of 40 Sv and the subpolar gyre has a transport of 13 Sv. We note that the sloped bathymetry significant alters the form of the subtropical gyre streamlines.

The depth-integrated vorticity diagnostics of the FLAT and SLOPED configuration are shown in Figures 7 and 8 respectively alongside the decomposition of the planetary vorticity diagnostic introduced in Section 3.4. In the FLAT configuration we note that the non-linear advection of vorticity and the planetary vorticity diagnostic have the largest grid point values ($\sim 10^{-9}\,\mathrm{m\ s^{-2}}$) near the western boundary currents of both gyres. The wind stress curl is one order of magnitude smaller ($\sim 10^{-10}\,\mathrm{m\ s^{-2}}$) but changes sign less frequently within the gyre regions. We see that the planetary vorticity diagnostic is almost entirely a result of the beta effect (Figure 7g and h). We note that the par-

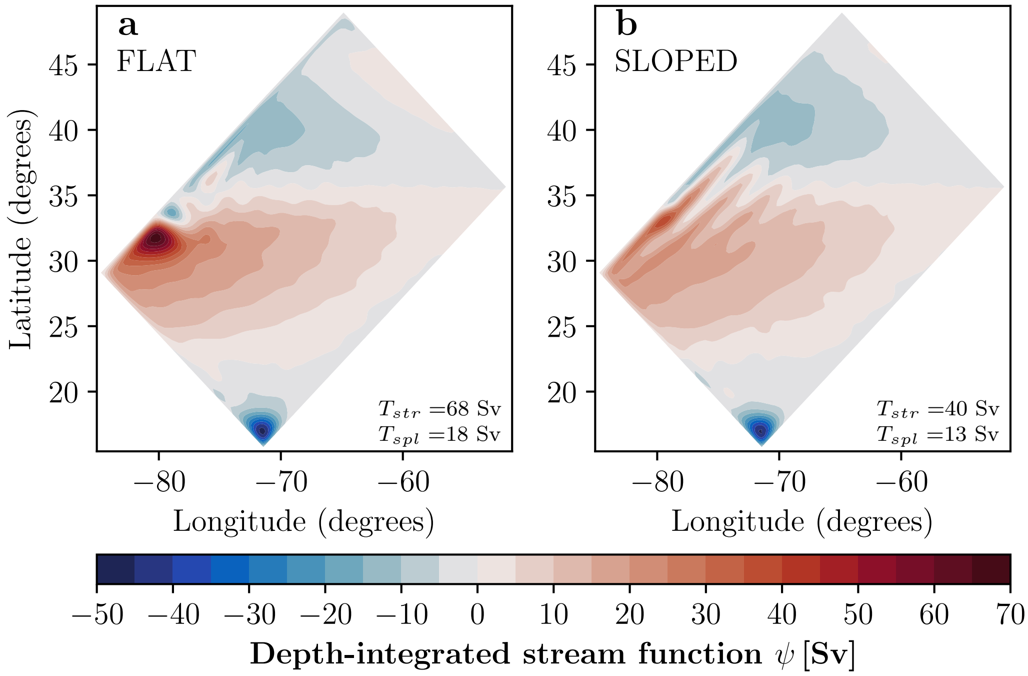

Figure 6. The depth-integrated streamfunction of the (a) FLAT and (b) SLOPED configurations. The transports of the subtropical gyre (T_{str}) and subpolar gyre (T_{spl}) are given.

tial cells contribution for the FLAT configuration is non-zero and localized to the edge (Figure 7j) where the EEN Coriolis scheme artificially shrinks F cell thicknesses near masked points.

In the SLOPED configuration (Figure 8) the advection and planetary vorticity diagnostics are still large but have an elongated structure similar to the SLOPED streamlines in Figure 6b. The bottom pressure torque is significant and is localized to the sloped region (Figure 8b). The planetary vorticity diagnostic has a more complex decomposition as the influence of partial cells extends beyond the edge of the domain and model level steps also contribute (Figure 8j).

The integrals of the vorticity diagnostics over areas enclosed by streamlines are shown in Figure 9 and Figure 10 for the FLAT and SLOPED configurations respectively as well as the integrals of the planetary vorticity diagnostic components. Example streamline contours are also shown. In these figures $\psi > 0$ describes the subtropical gyre and $\psi < 0$ describes the subpolar gyre. The subtropical and subpolar gyres circulate in the opposite direction but the sign of the integration results are adjusted so that positive integrals correspond to forces that spin the gyres up.

In the FLAT configuration we see that the subtropical and subpolar gyre are entirely driven by wind stress curl. At the exterior of the subtropical gyre (small and positive values of ψ) the wind stress curl is largely balanced by the advection of relative vorticity which implies a net import of positive vorticity into the gyre. The imported vorticity cannot originate from the subpolar gyre as the advection of relative vorticity plays no role in spinning the subpolar gyre down. Therefore the imported vorticity must originate from the recirculation gyre in the southernmost corner In the subtropical gyre interior the wind stress curl is largely balanced by the curl of bottom friction, matching the balance proposed by Niiler (1966).

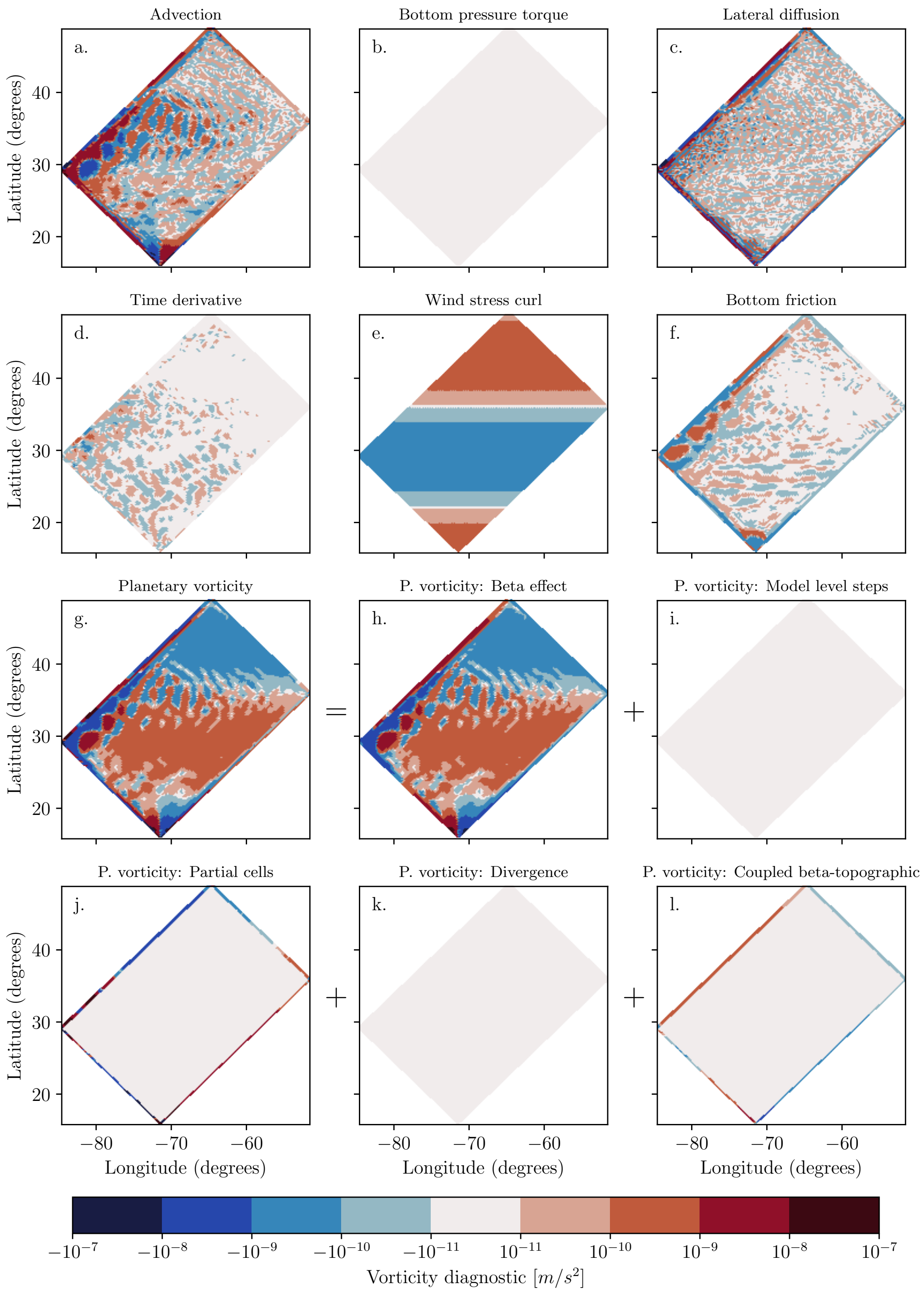

Figure 7. The depth-integrated vorticity diagnostics for the FLAT configuration and the components of the planetary vorticity diagnostic. The color bar is logarithmic (for values greater than 10^{-11} in magnitude) and shows the four leading order magnitudes that are positive and negative.

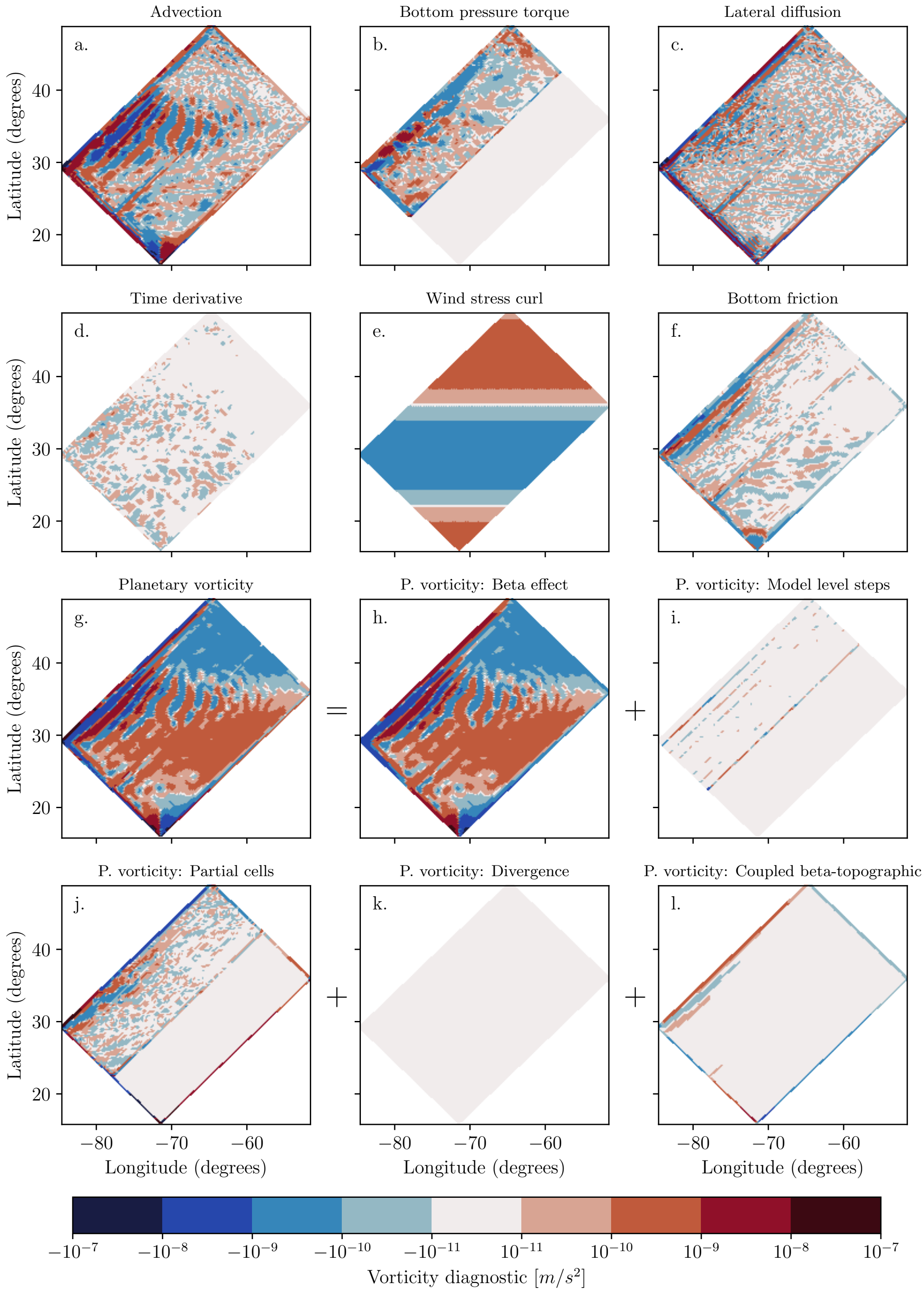

Figure 8. The depth-integrated vorticity diagnostics for the SLOPED configuration and the components of the planetary vorticity diagnostic.

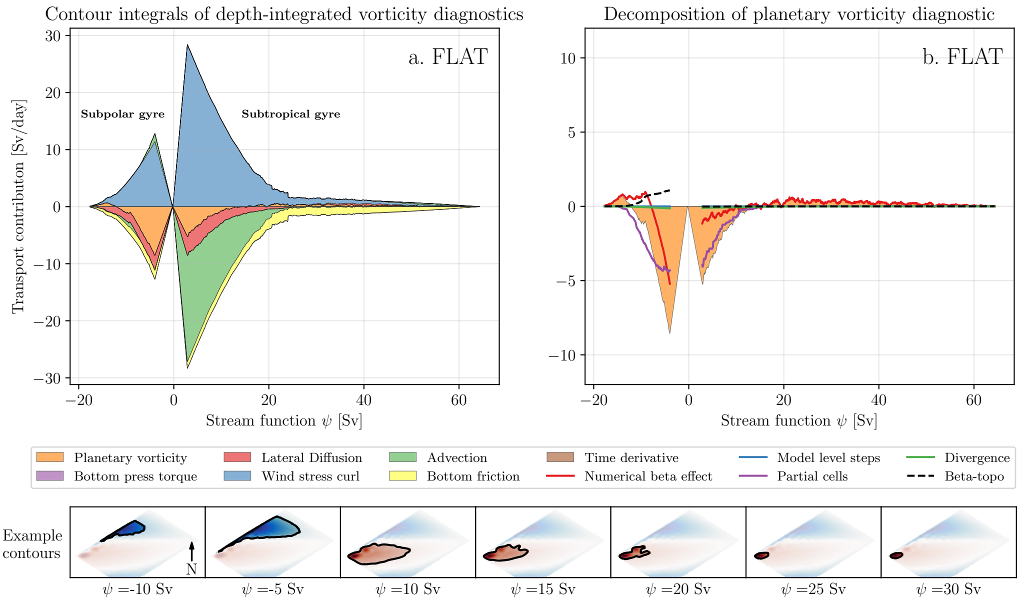

Figure 9. Stacked area plots showing the integrals of depth-integrated vorticity diagnostics for the FLAT configuration. Positive values correspond to a force that spins the subtropical ($\psi > 0$) or subpolar ($\psi < 0$) gyre up. The diagnostics are integrated over areas enclosed by streamlines to develop a full forcing profile of the gyres. The x axis describes the value of the streamline used in the integration. Example streamline contours are given. (b) Shows the area integrals of the planetary vorticity diagnostic and its components.

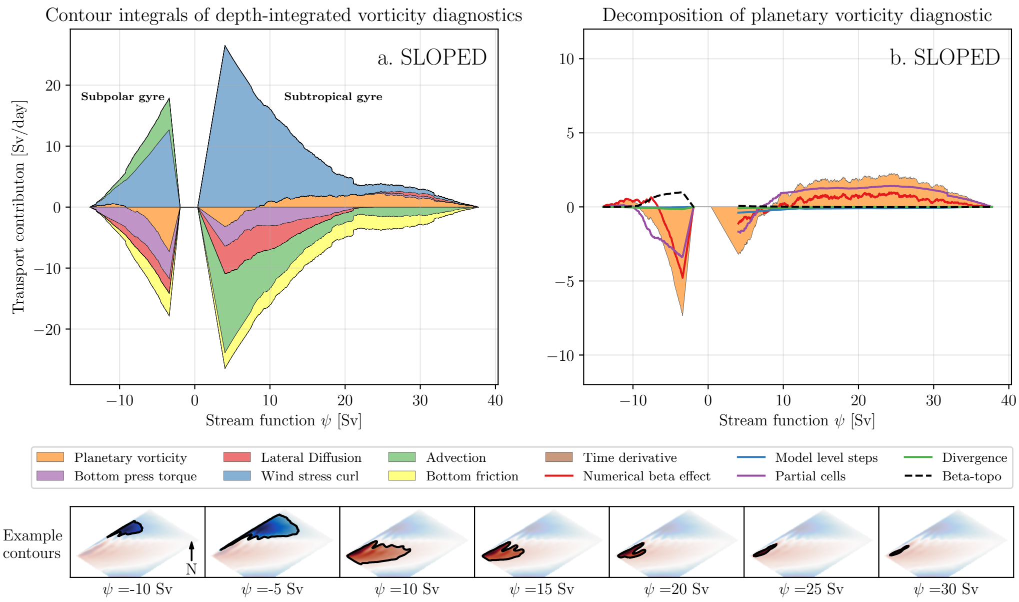

Figure 10. Stacked area plots showing the integrals of depth-integrated vorticity diagnostics for the SLOPED configuration. Positive values correspond to a force that spins the subtropical ($\psi > 0$) or subpolar ($\psi < 0$) gyre up. (b) Shows the area integrals of the planetary vorticity diagnostic and its components.

The planetary vorticity diagnostic is significant in both of the FLAT gyres and is the dominant drag for the subpolar gyre. At both gyre exteriors (small values of ψ) the integrated planetary vorticity diagnostic is a combined effect of the numerical beta effect discussed in Section 3.5 and the influence of partial F cells that are artificially created by the EEN scheme. At the interior of both gyres (large values of ψ) the numerical beta effect is the only component.

In the SLOPED configuration we see that both the subtropical and subpolar gyre are almost entirely driven by wind stress curl. There is no dominant force spinning the gyres down. Advection, bottom pressure torques, lateral diffusion, bottom friction, and planetary vorticity all make a similar contribution to spinning the gyres down. The planetary vorticity diagnostic is similarly mixed as both the beta effect and partial cells make up the signal. The gyres in the SLOPED configuration appear to be an intermediate case between a topographically steered gyre and an advective regime.

Spurious forces that emerge from the discrete Coriolis acceleration are significant in idealised models with and without variable bathymetry and appear to have a large influence on gyre circulations. In the next sub-section we see if these forces are also significant in a realistic global model.

5 The Weddell Gyre

5.1 Details of the configuration

We now consider a more realistic configuration based on the NEMO global model with realistic forcing and bathymetry. In this experiment, we use an ocean-ice global configuration that is similar to that described in (Storkey et al., 2018) but based on NEMO version 4. The global grid is based on the 'ORCA' family of grids within the NEMO framework (Madec et al., 2019). In this article we only consider the configuration using the ORCA025 grid (1/4° horizontal resolution at the equator). Most of the model bathymetry for ORCA025 is derived from the ETOPO1 data set (Amante & Eakins, 2009). Bathymetry on the Antarctic shelf is based on IBSCO (Arndt et al., 2013) and has been smoothed by three applications of a first order Shapiro filter. The bathymetry is represented in z-coordinates by partial cells (Bernard et al., 2006). Surface forcing is taken from the CORE2 surface forcing data set (Large & Yeager, 2009) and includes contributions from sea ice. The bathymetry is shown in Figure 11a.

The model uses a free slip boundary condition with a non-linear drag along the bottom boundaries and the TEOS-10 equation of state (McDougall & Barker, 2011). Biharmonic diffusion of momentum is implemented and acts along model level surfaces with a diffusivity that varies with local horizontal grid spacing (Willebrand et al., 2001). Laplacian diffusion of tracers is implemented and acts along isopycnal surfaces with a diffusivity that also varies with local horizontal grid spacing. The EEN vorticity scheme is used again for consistency with analysis in Section 3 and results in Section 4.

5.2 Methods

The methods used for calculating the depth-integrated streamfunction, vorticity diagnostics, and contour integrals are identical to those described in Section 4.2.

We study the area including and surrounding the Weddell Gyre in the model (see Figure 11) and consider the time-averaged fields over a typical year. The stream function is interpolated onto a regular 1/12° grid and closed contours are identified for 201 values of ψ. As we are studying a one gyre system we choose to only identify contours where $\psi > 0$. This effectively filters out the vorticity budget of the Antarctic Circumpolar Current. The sign of the integration results are adjusted so that positive integrals correspond to forces that spin the Weddell Gyre up.

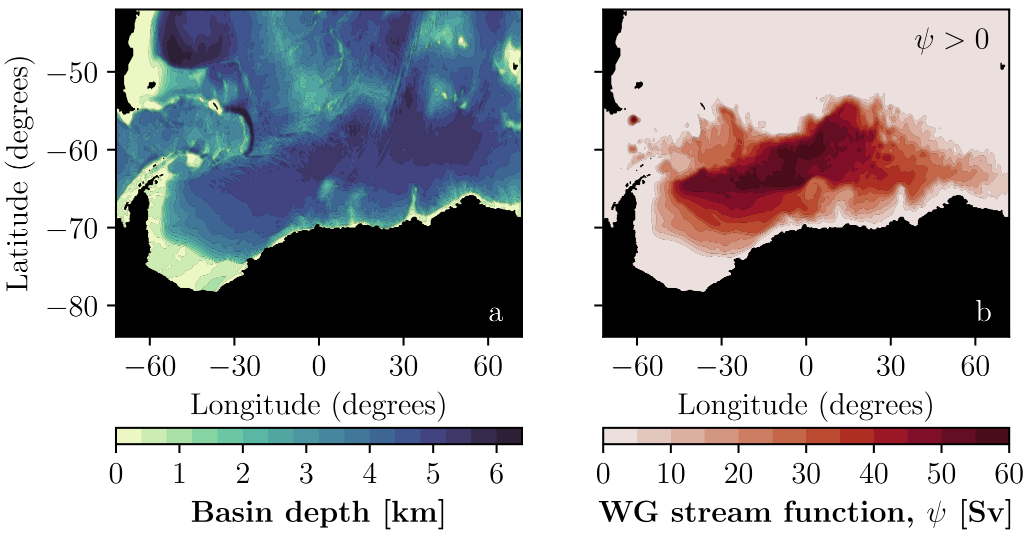

Figure 11. (a) The bathymetry of the Weddell Gyre region in the global model. (b) Depth-integrated streamfunction of the Weddell Gyre.

5.3 Results

The depth-integrated streamfunction of the Weddell Gyre is shown in Figure 11b and it can be seen that the Weddell Gyre has a transport of 60 Sv. The streamlines follow the isobaths closely suggesting the circulation is largely constrained by the bathymetry.

The depth-integrated vorticity diagnostics are shown in Figure 12. The combined effect of the wind stress and stress due to sea ice are shown in Figure 12e. With realistic topography and forcing, the grid point values of depth-integrated vorticity diagnostics are very noisy with the exception of the surface stress curl. This highlights how important the integrating area is when interpreting vorticity diagnostics. For individual grid points we see that the planetary vorticity diagnostic is made up of contributions from the beta effect, partial cells, and a significant contribution from model level steps. The beta effect is the most coherent of the contributions and is mostly negative in the western limb of the gyre where $\overline{v} > 0$ and positive in the eastern limb where $\overline{v} < 0$. As expected, the contribution from model levels steps is localized to areas where the number of model levels change.

Unlike in the double gyre model, bottom friction appears to be small and incoherent in the Weddell Gyre region and is unlikely to have any significant influence on the vorticity budget. The divergence of the depth-integrated budget is also small relative to the vorticity budget which suggests that the effect of fresh water input due to precipitation and sea ice is negligible. The total time tendency (Figure 12d) is non-zero in this vorticity budget suggesting that the model is not in a completely steady state; however, the grid point values are only significant in the Drake Passage and are noisy.

The integrals of the depth-integrated vorticity diagnostics over areas enclosed by streamlines are shown in Figure 13 alongside integrations of the planetary vorticity components. We see that the Weddell Gyre is almost entirely spun up by the wind stress curl. The stress due to sea ice (marked by hatching in Figure 13a) and the advection of relative vorticity also help to spin the Weddell Gyre up. The advective contribution is caused by vorticity exchange at the interface between the Weddell Gyre and the ACC.

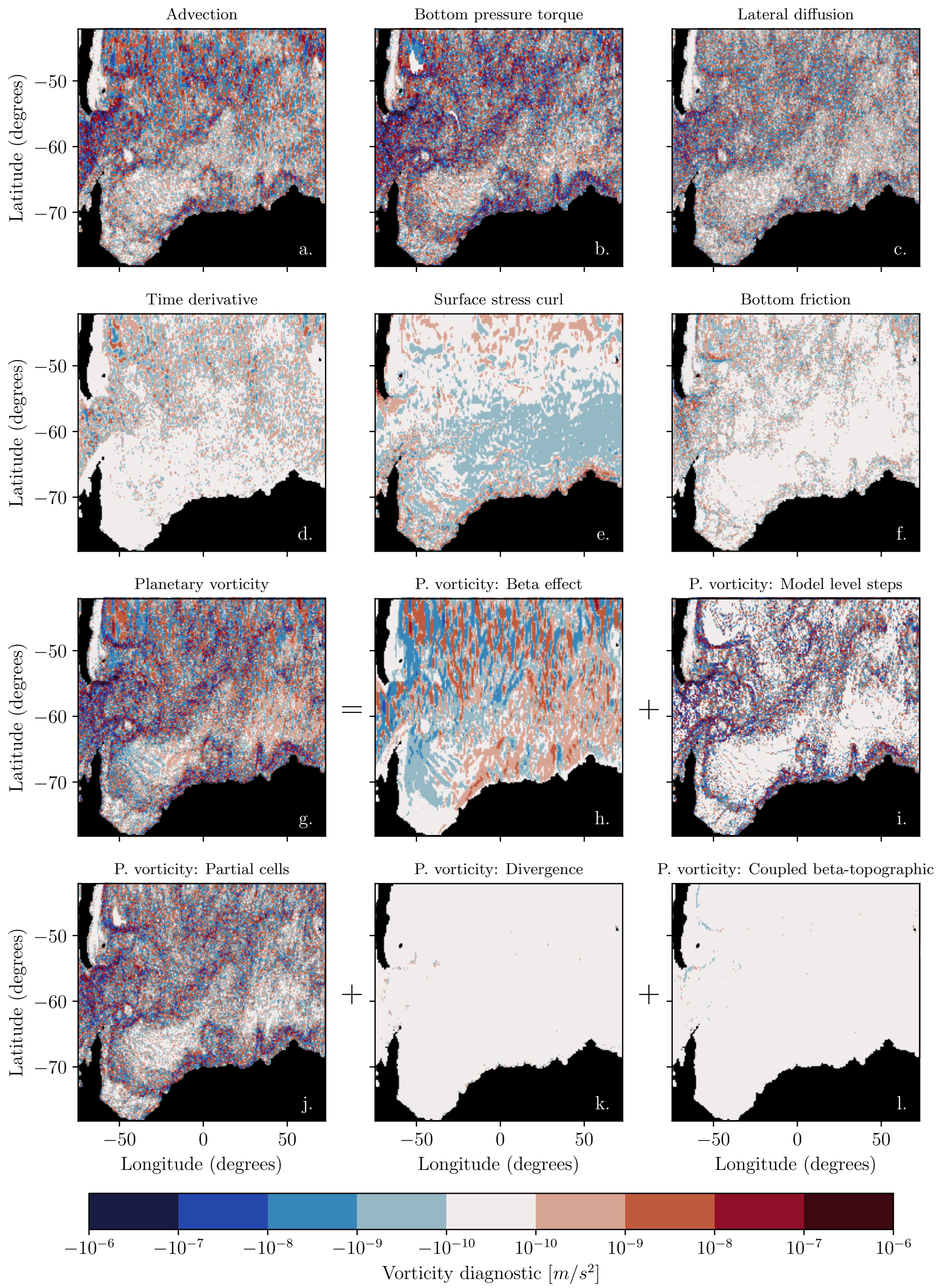

Figure 12. The depth-integrated vorticity diagnostics for the Weddell Gyre and the components of the planetary vorticity diagnostic.

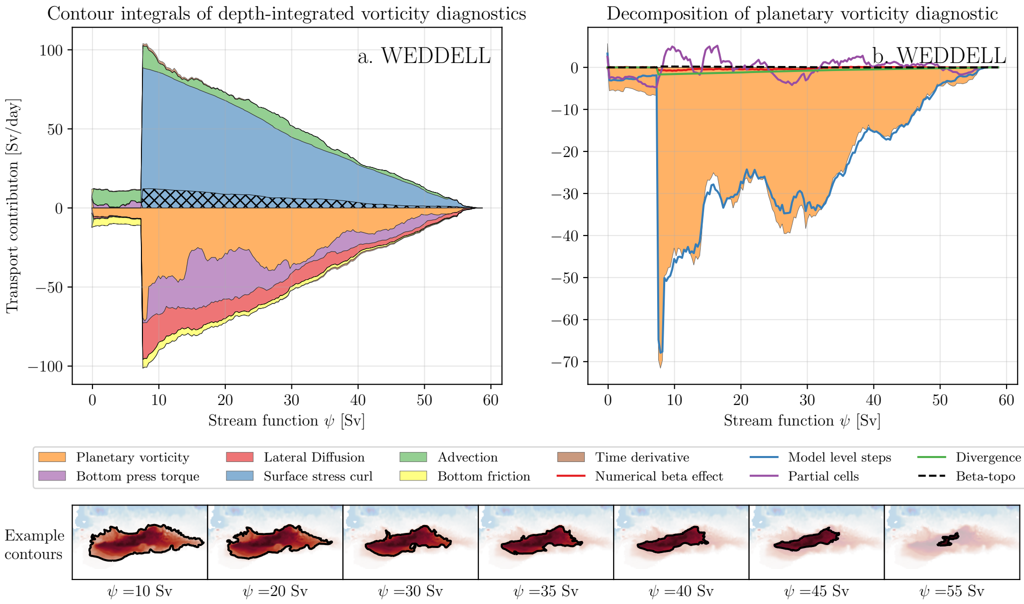

Figure 13. Stacked area plots showing the integrals of depth-integrated vorticity diagnostics for the Weddell Gyre. Positive values correspond to a force that spins the gyre up. The hatching marks the sea ice contribution to the surface stress integral. (b) Shows the area integrals of the planetary vorticity diagnostic and its components.

Bottom pressure torques and lateral diffusion play a notable role in spinning the Weddell Gyre down but the planetary vorticity diagnostic is the most significant contribution. Looking at the decomposition of the planetary vorticity diagnostic we see that the signal is mostly determined by changes in model level and the remainder is determined by partial cells. This suggests that the Weddell Gyre is almost entirely spun down by topography due to the combined effect of bottom pressure torques and the planetary vorticity diagnostic, but the majority of the gyre's interaction with the sea floor is spurious. This conclusion is true in both the interior and exterior of the gyre.

6 Discussion

We have shown that the vorticity dynamics of both highly idealized and realistic gyre configurations are greatly influenced by spurious forces that emerge from the discrete Coriolis force and the step-like representation of bathymetry. In the idealized double gyre configuration (Section 4) the spurious force is a combination of numerical beta and topographic effects that are present in both the FLAT and SLOPED configuration. In the realistic Weddell Gyre (Section 5) the spurious force is the dominant drag and is entirely determined by model level steps and partial cells. In this section we discuss possible methods to mitigate these spurious forces.

6.1 Alternative vorticity schemes

The results presented in Sections 4 and 5 both use the EEN vorticity scheme and it is tempting to dismiss the spurious forces as an artifact of the selected scheme. The analysis in Section 3.2 is general for three popular schemes: EEN, ENE, and ENS. The methods and decomposition used in this article are applicable under any scheme where the Coriolis acceleration can be expressed in the form of Equation 7. Results from the

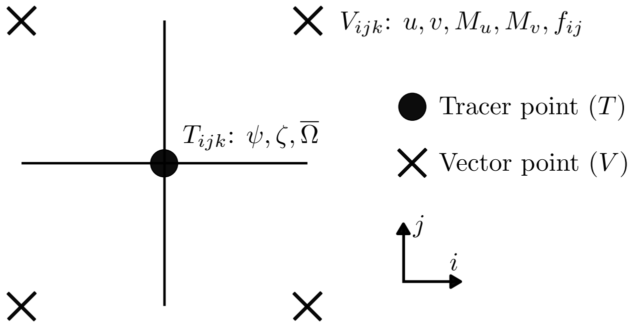

Figure 14. The horizontal distribution of variables on the B-grid. Tracer points (T) and vector points (V) are shown alongside important values that are centred on these points. Just like in the C-grid, the vertical velocities are found directly above and below the Tracer point.

SLOPED double gyre configuration using the different schemes are presented in Appendix B and the vorticity budgets are qualitatively similar. Spurious topographic forces and the numerical beta effect are still significant.

It therefore seems that switching between the available vorticity schemes will not alleviate the spurious signal. It is possible that a new scheme could be formulated which is designed to significantly reduce the spurious forces, but that will most likely require abandoning the conserved quantities that characterise the existing schemes.

6.2 The B-grid

Altering the grid geometry can significantly alter the behaviour of model forces. To highlight this we consider how the Coriolis force behaves on the B-grid.

The B-grid excels at representing geostrophic flows as f, u, and v are located on the same vector point. The streamfunction and relative vorticity are located on the tracer point as shown in Figure 14.

On the B-grid the Coriolis acceleration is simply:

$$\mathrm{COR}^x_{i,j,k} = f_{i,j}\, v_{i,j,k}, \tag{22}$$
$$\mathrm{COR}^y_{i,j,k} = -f_{i,j}\, u_{i,j,k}. \tag{23}$$

The Coriolis acceleration does not rely on multi-point averaging or thickness weighting of f so numerical contributions do not emerge in the grid point acceleration.

On the B-grid u and v lie on the same point so they share the same mask. This means that non-zero Coriolis accelerations are never masked near model level steps and the depth-integrated Coriolis acceleration is a function of the depth-integrated velocities only:

$$\overline{\mathrm{COR}}^x_{i,j} = f_{i,j}\, \overline{v}_{i,j}, \tag{24}$$
$$\overline{\mathrm{COR}}^y_{i,j} = -f_{i,j}\, \overline{u}_{i,j}. \tag{25}$$

We therefore conclude that the spurious force caused by model level steps on the C-grid (see Section 3.3) is not present on the B-grid.

In Appendix C we integrate the curl of the depth-integrated Coriolis acceleration over the area enclosed by a rectangular streamline which is analagous to the C-grid integration discussed in Section 3.5. The result of the B-grid integral is non-zero showing that $\iint_{A_\psi} \nabla_h \cdot (f\overline{\mathbf{u}}) \neq 0$ in general. This suggests that a numerical beta effect would still be present on the B-grid.

Using the B-grid would remove all of the spurious topographic forces identified in this article. This highlights how a model circulation's interaction with the sea floor is significantly affected by the grid geometry.

6.3 Terrain following coordinates

The spurious topographic effects found in this article are a consequence of how bottom topography is represented in z-coordinates. In the Weddell Gyre especially we see how model level steps can create large spurious contributions to the depth-integrated vorticity budget.

Terrain-following coordinates (or σ-coordinates) are an alternative form of vertical coordinate where the vertical resolution adjusts with the bottom topography so that the same number of model levels are present in all fluid columns (Song & Haidvogel, 1994). σ-coordinates are used in Stewart et al. (2021) and Schoonover et al. (2016) and have the advantage of removing spurious terms that emerge from model level steps. The forms of the EEN, ENE, and ENS vorticity schemes are unchanged when using terrain-following coordinates so the horizontal variations in cell thicknesses could still cause a spurious signal.

Terrain-following coordinates are not used widely in climate models because of the difficulty in calculating accurate horizontal pressure gradients (near the equator), advection, and isoneutral tracer advection. A full discussion of the current advantages and limitations of terrain following coordinates can be found in Lemarié et al. (2012).

7 Summary

The depth-integrated vorticity budget is a valuable tool for identifying important model forces in gyre circulations. Vorticity diagnostics can be integrated over the area enclosed by streamlines to identify forces responsible for spinning the gyre up and down. By considering how the vorticity budget is represented on a C-grid with step-like bathymetry we identified spurious forces that emerge from the representation of bottom topography and the discrete Coriolis acceleration. Model level steps and partial cells produce two distinct spurious topographic forces. A numerical beta effect emerges from the required multi-point averaging of the Coriolis parameter and remains when integrated over the area enclosed by gyre streamlines.

We first studied the vorticity budget of an idealized double gyre configuration with analytic geometry, forcing, and two bathymetry options. The FLAT variant has a constant depth and the SLOPED variant has a linear slope that extends over half the domain. The subtropical gyre of the FLAT configuration is non-linear at the exterior (wind stress curl balanced by advection) and is in a Stommel (1948) regime in the interior (wind stress curl balanced by friction). The FLAT subpolar gyre is spun up by wind stress curl and mostly spun down by spurious forces found in the planetary vorticity diagnostic. Spurious forces are significant in both FLAT gyres and are a consequence of the numerical beta effect and partial F cells that are artificially introduced by the EEN vorticity scheme. Artificial partial F cells would not be present in the ENS or ENE vorticity schemes.

The vorticity budget of the SLOPED gyres features bottom pressure torques and an increased influence of partial cells on the planetary vorticity diagnostic. The SLOPED subtropical gyre is an intermediate case between a topographically steered gyre and a non-linear circulation. The SLOPED subpolar gyre is driven by wind stress curl but spun down by the combined effect of bottom pressure torques and spurious interactions with the topography via partial F cells. This first case study highlighted how spurious terms can dominate a vorticity budget in simple configurations with and without variable bathymetry.

The second case study was the Weddell Gyre in a global model where the forcing and geometry are more realistic. By studying the vorticity budget of the Weddell Gyre we conclude that the model circulation is mostly spun up by wind stress curl and spun down by the combined effect of bottom pressure torques and spurious interactions with the topography. The largest of the topographic forces spinning the Weddell Gyre down is the spurious force caused by model level steps.

Switching to alternative vorticity schemes is not effective at reducing spurious contributions to the vorticity budget. By presenting a general form of the discrete Coriolis acceleration we are able to quickly conclude that the numerical beta effect and the influence of partial cells will remain under all three vorticity schemes and any other scheme that uses this general form. The influence of model level steps is a direct consequence of the C-grid geometry when using z-coordinates and is relatively insensitive to the choice of vorticity scheme.

Altering the geometry of the discretisation is an effective method for reducing spurious topographic forces. The B-grid is better at representing the Coriolis force and it is not possible for model level steps or partial cells to influence the Coriolis acceleration. Model level steps and their influence on the Coriolis acceleration can be avoided altogether by using terrain-following coordinates.

The B-grid and terrain-following coordinates have their own unique limitations and it is unclear how much the identified spurious forces corrupt circulation variables such as the gyre transport. It is possible that the spurious forces are inadvertently performing the role of one or more real ocean processes that are required for accurate simulations. If a combination of non-spurious forces can fully account for the spurious forces found in this article then the identified problem is purely diagnostic in nature. Otherwise, any part of the spurious forcing that cannot be accounted for by non-spurious forces should be considered as a numerical error. This numerical error could be small but may also accumulate under specific conditions and corrupt model circulations. The spurious cooling (Hecht, 2010) that occurs when a dispersive advection scheme is used with the Gent and McWilliams (1990) eddy parametrization highlights the dangers of ignoring numerical errors.

It is important for the ocean modelling community to continue developing new ways of representing bathymetry and we hope that vorticity budgets and the diagnostic method presented in this article will provide a valuable tool for assessing and quantifying representations of the sea floor in current and future ocean models.

Appendix A Explicit forms of the Coriolis schemes

Here we explicitly state the forms of the discrete Coriolis acceleration in the ENE, ENS, and EEN vorticity schemes for a z-coordinate system. In the ENE vorticity scheme the x and y components of the Coriolis acceleration are:

$$\begin{aligned}
\mathrm{COR}^x_{i,j,k} &= \frac{1}{4e^{1u}_{i,j}}\Big[f_{i,j-1}\left(\left(ve^{1v}\right)_{i,j-1,k}+\left(ve^{1v}\right)_{i+1,j-1,k}\right) \\
&\quad +f_{i,j}\left(\left(ve^{1v}\right)_{i,j,k}+\left(ve^{1v}\right)_{i+1,j,k}\right)\Big], \qquad \text{(A1)} \\
\mathrm{COR}^y_{i,j,k} &= \frac{1}{4e^{2v}_{i,j}}\Big[f_{i-1,j}\left(\left(ue^{2u}\right)_{i-1,j,k}+\left(ue^{2u}\right)_{i-1,j+1,k}\right) \\
&\quad +f_{i,j}\left(\left(ue^{2u}\right)_{i,j,k}+\left(ue^{2u}\right)_{i,j+1,k}\right)\Big]. \qquad \text{(A2)}
\end{aligned}$$

In the ENS vorticity scheme the x and y components of the Coriolis acceleration are:

$$\begin{aligned} \mathrm{COR}^x_{i,j,k} &= \frac{1}{8e^{1u}_{i,j}}\left[\left(ve^{1v}\right)_{i,j-1,k} + \left(ve^{1v}\right)_{i+1,j-1,k} \right. \\ &\quad \left. + \left(ve^{1v}\right)_{i,j,k} + \left(ve^{1v}\right)_{i+1,j,k}\right]\left[f_{i,j-1} + f_{i,j}\right], \qquad (A3) \\ \mathrm{COR}^y_{i,j,k} &= \frac{-1}{8e^{2v}_{i,j}}\left[\left(ue^{2u}\right)_{i-1,j-1,k} + \left(ue^{2u}\right)_{i-1,j+1,k} \right. \\ &\quad \left. + \left(ue^{2u}\right)_{i,j,k} + \left(ue^{2u}\right)_{i,j+1,k}\right]\left[f_{i-1,j} + f_{i,j}\right]. \qquad (A4) \end{aligned}$$

We note that each term in the ENE and ENS forms can be written in the general form of Equation 7 as $ve^{1v} = \tilde{V}/e^{3v}$ and $ue^{2u} = \tilde{U}/e^{3u}$. In the ENE and ENS cases $e^{3f}_k(\mathbf{b}_n) = e^{3v}_k(\mathbf{c}_n)$ for COR^x and $e^{3f}_k(\mathbf{b}_n) = e^{3u}_k(\mathbf{c}_n)$ for COR^y in Equation 7. In the EEN vorticity scheme, the x and y components of the Coriolis acceleration are:

$$\begin{aligned} \mathrm{COR}^x_{i,j,k} &= \frac{1}{12e^{1u}_{i,j}}\left[F^{NE}_{i,j,k}\left(ve^{3v}e^{1v}\right)_{i,j,k} + F^{NW}_{i+1,j,k}\left(ve^{3v}e^{1v}\right)_{i+1,j,k}\right. \\ &\quad \left. + F^{SE}_{i,j,k}\left(ve^{3v}e^{1v}\right)_{i,j-1,k} + F^{SW}_{i+1,j,k}\left(ve^{3v}e^{1v}\right)_{i+1,j-1,k}\right], \qquad (A5) \\ \mathrm{COR}^y_{i,j,k} &= \frac{-1}{12e^{2v}_{i,j}}\left[F^{NE}_{i,j,k}\left(ue^{3u}e^{2u}\right)_{i,j,k} + F^{NW}_{i,j,k}\left(ue^{3u}e^{2u}\right)_{i-1,j,k}\right. \\ &\quad \left. + F^{SE}_{i,j+1,k}\left(ue^{3u}e^{2u}\right)_{i,j+1,k} + F^{SW}_{i,j+1,k}\left(ue^{3u}e^{2u}\right)_{i-1,j+1,k}\right], \qquad (A6) \end{aligned}$$

where F^{NE}, F^{NW}, F^{SE}, and F^{SW} are thickness-weighted triads of the Coriolis parameter:

$$\begin{aligned} F^{NE}_{i,j,k} &= \left(\tilde{f}_{i,j,k} + \tilde{f}_{i-1,j,k} + \tilde{f}_{i,j-1,k}\right), \qquad (A7) \\ F^{NW}_{i,j,k} &= \left(\tilde{f}_{i,j,k} + \tilde{f}_{i-1,j,k} + \tilde{f}_{i-1,j-1,k}\right), \qquad (A8) \\ F^{SE}_{i,j,k} &= \left(\tilde{f}_{i,j,k} + \tilde{f}_{i,j-1,k} + \tilde{f}_{i-1,j-1,k}\right), \qquad (A9) \\ F^{SW}_{i,j,k} &= \left(\tilde{f}_{i-1,j,k} + \tilde{f}_{i,j-1,k} + \tilde{f}_{i-1,j-1,k}\right), \qquad (A10) \end{aligned}$$

where $\tilde{f} = f/e^{3f}$ using the EEN definition of e^{3f} shown in Equation 10.

To calculate the planetary vorticity diagnostic we take the curl of the depth-integrated Coriolis acceleration (defined in Equations 13 and 14):

$$\begin{aligned} \overline{\mathrm{PVO}}_{i,j} = \frac{1}{\left(e^{1f}e^{2f}\right)_{i,j,k}}\Bigg[&\left(\overline{\mathrm{COR}}^y e^{2v}\right)_{i+1,j} - \left(\overline{\mathrm{COR}}^y e^{2v}\right)_{i,j} \\ &- \left(\overline{\mathrm{COR}}^x e^{1u}\right)_{i,j+1} + \left(\overline{\mathrm{COR}}^x e^{1u}\right)_{i,j}\Bigg]. \qquad (A11) \end{aligned}$$

In general the resulting equation of the vorticity diagnostic is very difficult to interpret. We only present the form of the planetary vorticity diagnostic for the EEN scheme on a grid with no partial cells or model level steps as it is used to derive the numerical beta effect in Section 3.5:

$$\begin{aligned} \overline{\mathrm{PVO}}_{i,j} = \frac{1}{12\left(e^{1f}e^{2f}\right)_{i,j}}\Bigg[&-f^{NE}_{i,j+1}\left(Ve^{1v}\right)_{i,j+1} - f^{NW}_{i+1,j+1}\left(Ve^{1v}\right)_{i+1,j+1} \\ &+ f^{SE}_{i,j}\left(Ve^{1v}\right)_{i,j-1} + f^{SW}_{i+1,j}\left(Ve^{1v}\right)_{i+1,j-1} \\ &- f^{SE}_{i+1,j+1}\left(Ue^{2u}\right)_{i+1,j+1} - f^{NE}_{i+1,j}\left(Ue^{2u}\right)_{i+1,j} \\ &+ f^{SW}_{i,j+1}\left(Ue^{2u}\right)_{i-1,j+1} + f^{NW}_{i,j}\left(Ue^{2u}\right)_{i-1,j} \\ &- \left(f_{i,j+1} - f_{i,j-1}\right)\left(\left(Ve^{1v}\right)_{i+1,j} + \left(Ve^{1v}\right)_{i,j}\right) \\ &- \left(f_{i+1,j} - f_{i-1,j}\right)\left(\left(Ue^{2u}\right)_{i,j+1} + \left(Ue^{2u}\right)_{i,j}\right)\Bigg]. \qquad (A12) \end{aligned}$$

Appendix B Alternative vorticity schemes in the double gyre model

In this section we present various integrations of the SLOPED double gyre configuration using different vorticity schemes: EEN, ENS, and ENE. All other aspects of the experiment are as described in Section 4.1. The results are shown in Figure B1. The vorticity budget is qualitatively similar between the three cases as well as the decomposition of the planetary vorticity diagnostic. It should be noted that the circulations do differ as the transports vary and the separation points of the western boundary currents change.

Appendix C Contour integration on a B-grid

In this section we consider how the planetary vorticity diagnostic on a B-grid behaves when integrated over the area enclosed by a streamline. The example configuration used is analgous to the C-grid configuration in Section 3.5.

On a B-grid the relative vorticity is centred on the tracer point. As a result, the curl of the depth-integrated Coriolis acceleration depends on values of COR^x and COR^y on the four surrounding vector points. The resultant form of the planetary vorticity diagnostic is:

$$\begin{aligned}\overline{\mathrm{PVO}}_{i,j} = \frac{-1}{\left(e^{1t}e^{2t}\right)_{i,j}}\frac{1}{2} \quad \Big[\quad & \delta_i\left(f\overline{u}e^{2u}\right)_j + \delta_i\left(f\overline{u}e^{2u}\right)_{j-1} \\ & +\delta_j\left(f\overline{v}e^{1v}\right)_i + \delta_j\left(f\overline{v}e^{1v}\right)_{i-1}\Big],\end{aligned} \tag{C1}$$

where δ_i and δ_j are differencing operators that act along the i and j axes respectively:

$$\delta_i\left(A_{i,j}\right) = A_{i+1,j} - A_{i,j}, \tag{C2}$$

$$\delta_j\left(A_{i,j}\right) = A_{i,j+1} - A_{i,j}. \tag{C3}$$

The streamfunction is centred on B-grid tracer points and the associated incompressible flow can be calculated using the equations:

$$\overline{u}_{i,j} = -\frac{1}{2\Delta x}\left[\psi_{i,j+1} - \psi_{i,j} + \psi_{i+1,j+1} - \psi_{i+1,j}\right] \tag{C4}$$

$$\overline{v}_{i,j} = \frac{1}{2\Delta x}\left[\psi_{i+1,j} - \psi_{i,j} + \psi_{i+1,j+1} - \psi_{i,j+1}\right]. \tag{C5}$$

We consider a pen-and paper configuration that is shown in Figure C1. There are no topographic effects as we assume the grid has no partial cells or masked points. The external values of ψ are arbitrarily set to zero and the internal values are $\psi_{1,1} = 2\left(U_0 + U_1\right)\Delta x$ and $\psi_{2,1} = 2U_0\Delta x$ where Δx is the regular cell width. The velocity field is derived from ψ to guarantee an incompressible flow. If we integrate the planetary vorticity diagnostic over the area enclosed by a streamline where $0 < \psi < 2U_0\Delta x$ then the area integral is the sum of PVO over the two internal tracer points:

$$\begin{aligned} I(\psi) &= (\Delta x)^2\left[\overline{\mathrm{PVO}}_{2,2} + \overline{\mathrm{PVO}}_{3,2}\right] \\ &= U_1\Delta x\left(f_{2,2} - f_{2,1}\right). \end{aligned} \tag{C6}$$

Equation C6 is similar in form and magnitude to the C-grid result (Equation 21) and shows that a numerical beta effect can exist on a B-grid.

Appendix D Contour integration without interpolation

The interpolation of vorticity diagnostic fields and the streamfunction is discussed in Section 4.2. Linear interpolation is used to minimise edge effects in our contour integration but is not required. In this section we present results that use uninterpolated

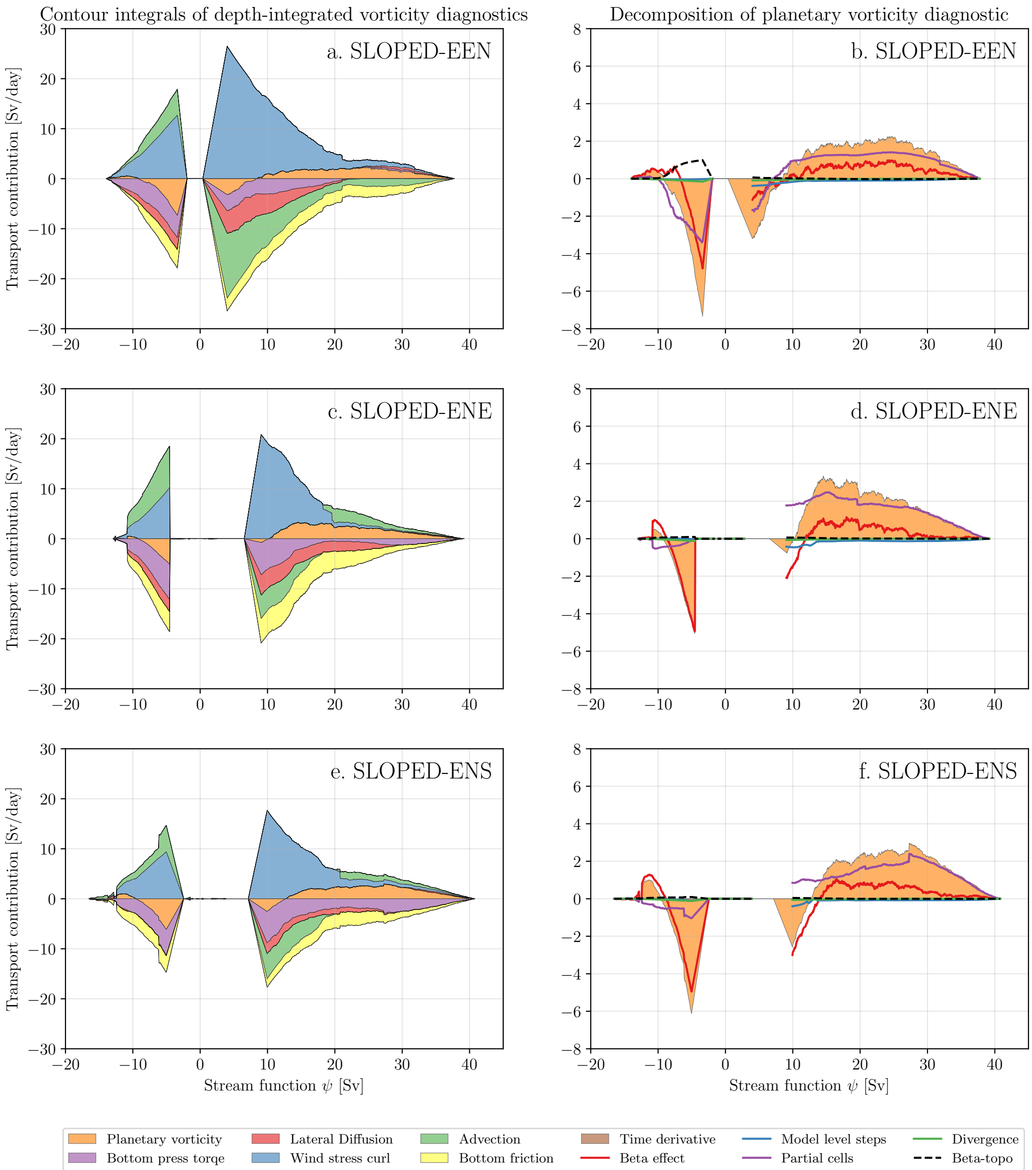

Figure B1. Stacked area plots showing the integrals of depth-integrated vorticity diagnostics for the SLOPED configuration using the EEN, ENE, and ENS vorticity schemes. Positive values correspond to a force that spins the subtropical ($\psi > 0$) or subpolar ($\psi < 0$) gyre up. A decomposition of the planetary vorticity diagnostic integrals are given on the RHS (b,d,f).

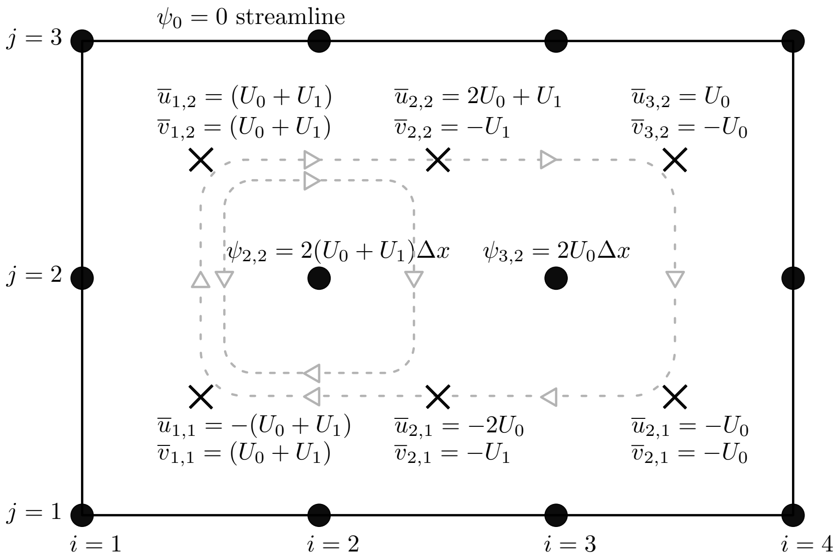

Figure C1. A simple flow on a B-grid where the planetary vorticity diagnostic does not integrate to zero when integrated within streamlines. The box is a rectangular streamline of value $\psi_0 = 0$. The flow is incompressible and calculated from the prescribed interior values of ψ. The background circulation is is illustrated by the gray dashed lines and is similar to the flow in Figure 4.

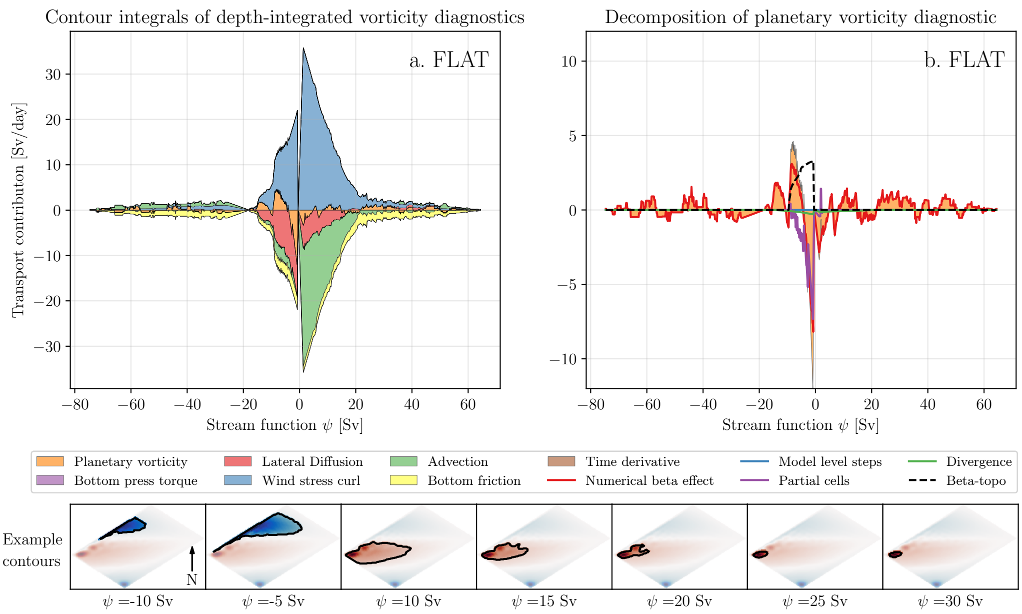

Figure D1. Stacked area plots showing the integrals of depth-integrated vorticity diagnostics for the SLOPED configuration without using interpolated fields. Positive values correspond to a force that spins the subtropical ($\psi > 0$) or subpolar ($\psi < 0$) gyre up. (b) Shows the area integrals of the planetary vorticity diagnostic and its components. The vorticity budget and decomposition are qualitatively similar to that shown in Figure 9.

fields from the FLAT double gyre configuration. The results are shown in Figure D1 and are qualitatively similar to the interpolated results shown in Figure 9. This example is selected to demonstrate both the qualitative similarity to interpolated results but also the reduced coherence that comes from using non-interpolated data. The non-interpolated results from the Weddell Gyre are in fact more coherent than the results shown in Figure D1.

Acknowledgments

This work was financially supported by the National Environment Research Council NE/S007474/1. This work used Monsoon2, a collaborative High-Performance Computing facility funded by the Met Office and the Natural Environment Research Council and used JASMIN, the UK collaborative data analysis facility. We would like to thank Julian Mak and Andrew Coward for their assistance in configuring NEMO on Monsoon2.

The software used to calculate, integrate, and plot the vorticity budget is available from https://github.com/afstyles/VorticityContourAnalysisForNemo/tree/1e8cc28/. The model integrations can be found on Zenodo (Styles et al., 2021).

The global configuration used in this article uses NEMO version 4.0.4 with the following merged branches:

- branches/UKMO/NEMO_4.0.4_mirror @ 14075,
- branches/UKMO/NEMO_4.0.4_GO8_package @ 14474,
- branches/UKMO/NEMO_4.0.4_GO6_mixing @ 14099,
- branches/UKMO/NEMO_4.0.4_old_tidal_mixing @ 14096,
- branches/UKMO/NEMO_4.0.4_momentum_trends @ 15194.

The double gyre configuration uses NEMO version 4.0.1 and any modified source code is archived on Zenodo (Styles et al., 2021). The versions of NEMO and the mentioned branches can be found at https://forge.ipsl.jussieu.fr/nemo/browser/NEMO/.

References

Amante, C., & Eakins, B. W. (2009). ETOPO1 arc-minute global relief model: procedures, data sources and analysis. *NOAA Technical Memorandum NESDIS NGDC-24*.

Arakawa, A., & Lamb, V. R. (1981). A potential enstrophy and energy conserving scheme for the shallow water equations. *Monthly Weather Review*, *109*(1), 18–36.

Arndt, J. E., Schenke, H. W., Jakobsson, M., Nitsche, F. O., Buys, G., Goleby, B., ... Wigley, R. (2013, jun). The International Bathymetric Chart of the Southern Ocean (IBCSO) Version 1.0-A new bathymetric compilation covering circum-Antarctic waters. *Geophysical Research Letters*, *40*(12), 3111–3117. doi: 10.1002/grl.50413

Bell, M. J. (1999). Vortex stretching and bottom torques in the Bryan-Cox ocean circulation model. *Journal of Geophysical Research: Oceans*. doi: 10.1029/1999jc900064

Bernard, B., Madec, G., Penduff, T., Molines, J. M., Treguier, A. M., Le Sommer, J., ... De Cuevas, B. (2006). Impact of partial steps and momentum advection schemes in a global ocean circulation model at eddy-permitting resolution. *Ocean Dynamics*, *56*(5-6), 543–567. doi: 10.1007/s10236-006-0082-1

Bras, I. A. A. L., Sonnewald, M., & Toole, J. M. (2019, nov). A barotropic vorticity budget for the subtropical north atlantic based on observations. *Journal of Physical Oceanography*, *49*(11), 2781–2797. doi: 10.1175/JPO-D-19-0111.1

Cane, M. A., Kamenkovich, V. M., & Krupitsky, A. (1998). On the utility and disutility of JEBAR. *Journal of Physical Oceanography*. doi: 10.1175/1520-0485(1998)028⟨0519:OTUADO⟩2.0.CO;2

Drijfhout, S. S., Marshall, D. P., & Dijkstra, H. A. (2013). Conceptual Models of the Wind-Driven and Thermohaline Circulation. In G. Siedler, S. M. Griffies, J. Gould, & J. A. Church (Eds.), *Ocean circulation and climate* (Vol. 103, pp. 257–282). Academic Press. doi: 10.1016/B978-0-12-391851-2.00011-8

Gent, P. R., & McWilliams, J. C. (1990). Isopycnal Mixing in Ocean Circulation Models. *Journal of Physical Oceanography*. doi: 10.1175/1520-0485(1990)020⟨0150:imiocm⟩2.0.co;2

Hecht, M. W. (2010, jan). Cautionary tales of persistent accumulation of numerical error: Dispersive centered advection. *Ocean Modelling*, *35*(3), 270–276. doi: 10.1016/j.ocemod.2010.07.005

Large, W. G., & Yeager, S. G. (2009, aug). The global climatology of an interannually varying air - Sea flux data set. *Climate Dynamics*, *33*(2-3), 341–364. doi: 10.1007/s00382-008-0441-3

Le Corre, M., Gula, J., & Tréguier, A. M. (2020). Barotropic vorticity balance of the North Atlantic subpolar gyre in an eddy-resolving model. *Ocean Science*. doi: 10.5194/os-16-451-2020

Lemarié, F., Kurian, J., Shchepetkin, A. F., Jeroen Molemaker, M., Colas, F., & McWilliams, J. C. (2012). Are there inescapable issues prohibiting the use of terrain-following coordinates in climate models? *Ocean Modelling*, *42*, 57–79. doi: 10.1016/j.ocemod.2011.11.007

Lévy, M., Jahn, O., Dutkiewicz, S., Follows, M. J., & D'Ovidio, F. (2015). The dynamical landscape of marine phytoplankton diversity. *Journal of the Royal Society Interface*. doi: 10.1098/rsif.2015.0481

Lévy, M., Klein, P., Tréguier, A. M., Iovino, D., Madec, G., Masson, S., & Takahashi, K. (2010). Modifications of gyre circulation by sub-mesoscale physics. *Ocean Modelling*, *34*(1-2), 1–15. doi: 10.1016/j.ocemod.2010.04.001

Madec, G., Bourdallé-Badie, R., Chanut, J., Samson, E. C., Coward, A., Ethé, C., … Samson, G. (2019, oct). *NEMO ocean engine.* Zenodo. doi: 10.5281/zenodo.1464816

McDougall, T. J., & Barker, P. M. (2011). Getting started with TEOS-10 and the Gibbs Seawater (GSW) oceanographic toolbox. *SCOR/IAPSO WG*, *127*, 1–28. Retrieved from https://www.teos-10.org/

Mesinger, F., & Arakawa, A. (1976). Numerical methods used in atmospheric models. *GARP Publications Series, 17 . Global Atmospheric Research Programme (GARP), 64 pp.*.

Niiler, P. P. (1966, aug). On the theory of wind-driven ocean circulation. *Deep-Sea Research and Oceanographic Abstracts*, *13*(4), 597–606. doi: 10.1016/0011-7471(66)90591-2

Perezhogin, P. (2019). Deterministic and stochastic parameterizations of kinetic energy backscatter in the NEMO ocean model in Double-Gyre configuration. In *Iop conference series: Earth and environmental science.* doi: 10.1088/1755-1315/386/1/012025

Ruggiero, G. A., Ourmières, Y., Cosme, E., Blum, J., Auroux, D., & Verron, J. (2015). Data assimilation experiments using diffusive back-and-forth nudging for the NEMO ocean model. *Nonlinear Processes in Geophysics*. doi: 10.5194/npg-22-233-2015

Sadourny, R. (1975). The Dynamics of Finite-Difference Models of the Shallow-Water Equations. *Journal of Atmospheric Sciences*, *32*(4), 680–689. doi: 10.1175/1520-0469(1975)032⟨0680:TDOFDM⟩2.0.CO;2

Schoonover, J., Dewar, W., Wienders, N., Gula, J., McWilliams, J. C., Molemaker, M. J., … Yeager, S. (2016). North Atlantic barotropic vorticity balances in numerical models. *Journal of Physical Oceanography*. doi: 10.1175/JPO-D-15-0133.1

Song, Y., & Haidvogel, D. (1994). A Semi-implicit Ocean Circulation Model Using a Generalized Topography-Following Coordinate System. *Journal of Computational Physics*, *115*(1), 228–244. doi: 10.1006/jcph.1994.1189

Stewart, A. L., McWilliams, J. C., & Solodoch, A. (2021). On the Role of Bottom Pressure Torques in Wind-Driven Gyres. *Journal of Physical Oceanography*, *51*(5), 1441–1464. doi: 10.1175/jpo-d-20-0147.1

Stommel, H. (1948). The westward intensification of wind-driven ocean currents. *Eos, Transactions American Geophysical Union*. doi: 10.1029/TR029i002p00202

Storkey, D., Blaker, A. T., Mathiot, P., Megann, A., Aksenov, Y., Blockley, E. W., ... Sinha, B. (2018, aug). UK Global Ocean GO6 and GO7: A traceable hierarchy of model resolutions. *Geoscientific Model Development*, *11*(8), 3187–3213. doi: 10.5194/gmd-11-3187-2018

Styles, A. F., Bell, M. J., Marshall, D. P., & Storkey, D. (2021). *Data for "Spurious topographic forces can dominate the vorticity budget of ocean gyres on the C-grid"*. Zenodo. doi: 10.5281/zenodo.5513825

Vallis, G. K. (2017). Atmospheric and oceanic fluid dynamics: Fundamentals and large-scale circulation, second edition. *Atmospheric and Oceanic Fluid Dynamics: Fundamentals and Large-Scale Circulation, Second Edition*, 1–946. doi: 10.1017/9781107588417

Van Der Walt, S., Schönberger, J. L., Nunez-Iglesias, J., Boulogne, F., Warner, J. D., Yager, N., ... Yu, T. (2014, jun). Scikit-image: Image processing in python. *PeerJ*, *2014*(1), e453. doi: 10.7717/peerj.453

Willebrand, J., Barnier, B., Böning, C., Dieterich, C., Killworth, P. D., Le Provost, C., ... New, A. L. (2001, jan). Circulation characteristics in three eddy-permitting models of the North Atlantic. *Progress in Oceanography*, *48*(2-3), 123–161. doi: 10.1016/S0079-6611(01)00003-9